Piezoelectric Energy Harvesting From Flutter

By

Soroush Norouzi

B.Sc. (Mechanical Engineering), University of Tehran, 2009

Thesis Submitted in Partial Fulfillment
of the Requirements for the Degree of
Master of Applied Science

in the
School of Engineering Sciences
Faculty of Applied Sciences

© Soroush Norouzi 2013

SIMON FRASER UNIVERSITY

Spring 2013

All rights reserved.
However, in accordance with the *Copyright Act of Canada*, this work may be reproduced, without authorization, under the conditions for "Fair Dealing." Therefore, limited reproduction of this work for the purposes of private study, research, criticism, review and news reporting is likely to be in accordance with the law, particularly if cited appropriately.

Approval

Name: **Soroush Norouzi**

Degree: **Master of Applied Science**

Title of Thesis: ***Piezoelectric Energy Harvesting From Flutter***

Examining Committee:

Chair: Dr. Erik Kjeang
Assistant Professor
Mechatronic Systems Engineering

Dr. Siamak Arzanpour
Senior Supervisor
Assistant Professor
Mechatronic Systems Engineering

Dr. Gary Wang
Supervisor
Professor
Mechatronic Systems Engineering

Dr. Mehrdad Moallem
Internal Examiner
Professor
Mechatronic Systems Engineering

Date Defended/Approved: December 11th , 2012

Partial Copyright License

The author, whose copyright is declared on the title page of this work, has granted to Simon Fraser University the right to lend this thesis, project or extended essay to users of the Simon Fraser University Library, and to make partial or single copies only for such users or in response to a request from the library of any other university, or other educational institution, on its own behalf or for one of its users.

The author has further granted permission to Simon Fraser University to keep or make a digital copy for use in its circulating collection (currently available to the public at the "Institutional Repository" link of the SFU Library website (www.lib.sfu.ca) at http://summit/sfu.ca and, without changing the content, to translate the thesis/project or extended essays, if technically possible, to any medium or format for the purpose of preservation of the digital work.

The author has further agreed that permission for multiple copying of this work for scholarly purposes may be granted by either the author or the Dean of Graduate Studies.

It is understood that copying or publication of this work for financial gain shall not be allowed without the author's written permission.

Permission for public performance, or limited permission for private scholarly use, of any multimedia materials forming part of this work, may have been granted by the author. This information may be found on the separately catalogued multimedia material and in the signed Partial Copyright Licence.

While licensing SFU to permit the above uses, the author retains copyright in the thesis, project or extended essays, including the right to change the work for subsequent purposes, including editing and publishing the work in whole or in part, and licensing other parties, as the author may desire.

The original Partial Copyright Licence attesting to these terms, and signed by this author, may be found in the original bound copy of this work, retained in the Simon Fraser University Archive.

Simon Fraser University Library
Burnaby, British Columbia, Canada

revised Fall 2011

Abstract

With the increasing need for alternative sources of energy, a great deal of attention is drawn to harvesting energy from ambient vibration. These vibrations may be caused by fluid forces acting upon a structure. When a flexible structure is subject to a fluid flow, it loses stability at a certain flow velocity and starts to vibrate. This self-induced motion is called flutter where energy is continuously transferred from the fluid to the structure. In this study a piezoelectric film sensor is used as a fluttering object, to convert the motion to electrical energy, and the energy harvesting capacity of the proposed concept is investigated. An experimental setup, composed of data acquisition methods, is designed and the findings are validated by original test data. The results are also compared to similar literature and it is concluded that the proposed energy harvesting technique meets the requirements of the intended application.

- **Keywords**: Flow-Induced Vibrations, Flutter, Piezoelectricity, Energy Harvesting

To Mom, Dad, Brother

Acknowledgements

First and foremost, I send my deepest gratitude to my family; the absolute source of love and support, who have always had the most faith in me, even when I had the least.

I would like to thank my supervisor, Dr. Siamak Arzanpour, for affording me the opportunity of working in his research group. He has taught me lessons, in science and life alike, which I hold of utmost value. I am very grateful for all his guidance and support, for this work could not have been completed without them. I would also like to thank Dr. Gary Wang for the support and care he offered me, both professionally and personally. I thank Dr. Mehrdad Moallem, my examiner, for accepting to read and evaluate this thesis

Special thanks go to my friend and companion, Maryam Hamidirad, who has been the light in the dark, and the warm in the cold. I express my highest appreciation for her love and support.

I thank my friends and lab mates. I hold dearest the time we shared, and the talk.

Finally, I would like to thank me, who kept at it.

Table of Contents

List of Figures

Chapter 1:

Introduction

Motivation

In light of the drastic advancements in electronics technology throughout the past couple of decades, a paradigm change has been happening in various fields of engineering. A major distinction between the new generation of measurement systems and their predecessors is the built-in intelligence as a result of employing a sensor network, controllers and data transmission apparatus. Thanks to light-weight and low-powered radio transmitters, sensors can now be placed in remote locations and provide live data on various mechanical properties of systems such as pressure, temperature, etc. The wireless nature of these measurement devices is in accordance with the demand for minimizing the use of material, reducing cost and saving energy. However to take full advantage of these opportunities a reliable long-lasting source of electric power must be available to keep these devices operating. This is challenging because the wireless sensor networks are basically intended for use in remote locations where the wiring needed for power distribution is not available. Therefore the concept of localized power sources is considered as a potential solution.

One possible substitute for central powering in sensor networks and data transmission units is to use batteries. The disadvantage of this solution, however, is that batteries have a limited lifespan and it is not always feasible or even possible to have access for battery replacement or recharging after they are in place. In gas pipelines, for example, neither central nor battery power transmission is desirable because cutting the surface of the pipe to pass wires or provide access for battery replacement will require extra safety

considerations to avoid any leakage. On the other hand, such a system will require frequent maintenance which would be very expensive in the case of pipelines that extend for hundreds of kilometres. These issues will make batteries an unfeasible solution for applications that are meant to perform over extended periods of time.

An alternative approach is to locally generate the needed electricity relying on the ambient energy. This approach has been adopted in wrist watches and some other cases for a long time and is called Energy Harvesting. Since a major application of sensors is measuring mechanical properties, some form of mechanical energy usually exists in the surroundings that can be harnessed and converted to electricity by means of an electromechanical transducer. The generated electrical power may then be used directly to power the equipment or to help recharge the battery to prolong its lifespan. For example, when pressure is being measured on a pipeline, the fluid within the pipe carries a kinetic energy due to its flow. This motion can be transferred to an electromechanical transducer, where energy conversion can happen.

There are a number of options for converting mechanical motion into electricity. Electromagnetic conversion is one of the most common techniques, where the motion of a coil inside a magnetic field induces an electric current in the coil. This method is widely used in power plants as well as low-power energy harvesters [1], but one disadvantage is the design complexity, of such systems with multiple parts, e.g. coil, magnet, slider, etc., required to work in harmony. This will lead to more difficult design which is also not suitable for small size applications. Another approach is using piezoelectric materials that generate an electric field in response to an applied mechanical stress. These materials are widely used in vibration-based energy harvesters due to their simplicity of use and high power generation capacity [1]. In general, the choice of a proper transduction method depends mainly on the mechanics of the problem in terms of the ambient energy and how it can be transferred to the transducer.

In this thesis we aim to find an energy harvesting solution where the source of ambient energy is a moving fluid. To that end, a review of the relevant literature is first conducted to understand the characteristic of the situation and identify different potential approaches for energy conversion and their cost and benefit. This knowledge will then be used to proceed to designing the energy harvester.

Literature Review

Energy Harvesting From Fluid Flow

Windmills are well-known clean energy power generators that have been around for many years to convert wind power to electricity. These devices are expensive and are only economically recommended where sufficient wind power is available and preferable not located close to where people live. Moreover, windmills have significant maintenance costs and as a result they will be only allowed to operate when the efficiency is above a threshold. In an attempt to find an alternative for windmills, Adamko and DeLaurier [2] and McKinney and DeLaurier [3] proposed the idea of an oscillating-wing windmill (wingmill). This device consists of a series of airfoil-shaped “wings” that are sequentially attached and placed in a fluid flow. The flapping of these wings due to the fluid flow is then converted to rotary motion that is transferred to an electromagnetic generator. Despite the original idea to use this device as a wind power generator, it can also work with water in rivers where building a dam is not feasible. Ly and Chasteau [4] demonstrated that the wingmill can achieve efficiency equal to a vertical axis wind turbine [5].

It is to be noted that the portion of the entire available power that wind turbines capture is limited to Betz limits [6] of 33% and 59% for vertical and horizontal axis configurations, respectively [7]. Therefore, for the purpose of energy harvesting where ample ambient energy is not always available, only low-powered energy harvesters can be made using the conventional turbine-generator configuration. For example, Weimar et al. [7] employed an anemometer to transfer wind power to a small-scale generator and provide an

energy source for low-power autonomous sensors. Their design was able to achieve up to 80% conversion efficiency with output powers limited to 700 microwatts. Although the main goal of the wingmill was to compete with conventional wind turbines, it was one of the first approaches to use flow-induced vibrations as a source for electricity generation. Meanwhile, the majority of energy harvesting research consists of vibration-based devices that work with an external oscillatory vibration with low amplitude and constant frequency [8]. Flow-induced vibrations could be used as a source of mechanical energy in situations where a fluid flow is present

In the past, flow-induced vibrations were considered unwanted and destructive in design problems such as aircraft wings or long bridges. It is because the interactions between the structure and its surrounding fluid can grow to such large amplitude vibrations that over time can lead to serious damage and failure of the structure. Despite this harmful nature of flow-induced vibrations, there have been attempts to benefit from the huge energy content of these vibrations to generate electricity.

The energy-harvesting eel is one the methods, proposed by Allen and Smits [9] and Taylor et al [10], for fluid-induced vibration energy harvesting. This device comprises of a flexible piezoelectric polymer film placed in a wake, generated from an upstream bluff body. The turbulences caused by the object vibrate the film. Due to the piezoelectric effect, electric charge is generated in response to the stresses associated with this vibration. This energy-harvesting concept can provide an electricity source to power remote sensors. This idea has already been patented by Carrol [11] while researchers are still trying to improve the device's electrical output and efficiency. Another interesting design of a flow-induced vibration energy-harvesting device is “windbelt” which has recently been patented and manufactured by Humdinger Wind Energy, LLC [12]. A windbelt is a properly tensioned flexible belt placed in airflow. The main difference between this design and the energy harvesting eel is the three-dimensional deformation of the flexible belt. A similar device is also proposed by Vortex Oscillating Technology, Ltd. [13].

Another source of vibration which has not been widely considered for energy harvesting is flutter. Flutter initiates when a fluid flow passes over a flexible structure (e.g., a cantilever beam) and the fluid pressure force on the structure causes it to deflect. Then, the elasticity of the structure counters these forces and creates a dynamic interaction with the fluid. If the stiffness of the structure suffices to resist substantial deformation, the system can stay in balance. For higher flow-induced forces, however, the deformations can grow to a point that the geometry of the flow field is significantly altered, thus complicating the dynamics of the system. At a certain *critical flow velocity*, the structure loses its stability and starts to vibrate. Once the stability is lost, the oscillations will constantly be fuelled by the energy of the moving fluid. This type of persistent vibration is referred to as *flutter*, and can be seen in various scenarios from the waving motion of flags, to the buzzing reeds in a Clarinet. The self-induced and continuous nature of flutter creates an opportunity for energy harvesting in situations where a constant ambient flow is present. A recent study by Tang et al., [14] investigated the energy transfer between the plate and the surrounding fluid flow based on which they propose the concept of a new energy-harvesting device, called “flutter-mill” [15]. In that study, however, the flutter-mill benefits from an electromagnetic transduction scheme, therefore sophisticated design and multiple parts are required. A different design concept was introduced by Bryant and Garcia [16] by placing an airfoil in a flow and transferring the flutter vibrations to a piezoelectric ceramic (PZT) by means of linkages. Erturk et al. [17] performed an experimental study investigating the output power and the effect of energy harvesting on the flutter dynamics of the airfoil. The first one to use a simplistic design was Kwon [18] who studied a T-shaped energy harvester that worked in a cross flow orientation. This device used a PZT mounted on a larger substrate, so that the fluttering would lead to power generation by the PZT.

Flutter seems to be a promising approach of energy harvesting for the remote sensor networks that motivated this research study. To better benefit from flutter in energy harvesting from fluid flow an investigation about the phenomena and the parameter involved is essential.

Flutter: a Flow-Induced Vibration

The earliest literature on flutter is of the experiments conducted by Taneda [19] who studied the flutter of hanging strips. He used linear models to investigate the instabilities of strips in air flow. Later on, Datta and Gottenberg [20] tried to propose a theoretical prediction of the critical velocity (minimum flow velocity required for flutter to take place) in terms of strip dimensions based on a similar series of experiments. Neglecting the nonlinearities in the system, both of these studies combined Euler-Bernoulli and Slender Wing [21] theories for modeling the structure and the fluid behaviour, respectively. They found the linear model to be able to predict the stability threshold with acceptable consistency with test data. In a more recent research, Lemaitre et al. [22], motivated by their experimental observations, followed the same theoretical approach to investigate the potential independence of the critical velocity from strip length for long hanging strips. They found that critical velocity decreases for longer strips until it reaches a final value. The first group to study the plates in a vertical/horizontal configuration were Kornecki et al. [23] who, instead of using slender wind theory, assumed a potential flow with zero circulation and added a distribution of vorticity on the plate using Theodorsen's theory [24] to account for the two-dimensional flow. Meanwhile, Argentina and Mahadevan [25] investigated the flutter mechanism of cantilevered plates in axial flow by means of a simplified analytical model based on Theodorsen's theory. To further advance the fluid modeling, Balint and Lucey [26] employed a Navier-Stokes solver in their attempt to provide a treatment for human snoring, which is the flutter of the palate. They found a mechanism of irreversible energy transfer from the fluid to the structure supporting the self-induced and continuous nature of this phenomenon.

The flutter stability conditions of structures have been theoretically and experimentally studied in a number of research projects, benefiting from the accuracy linear models can provide for determining the critical velocity. Analyzing the three-dimensional stability, Shayo [27] concluded that a flag of infinite span is more stable than a finite one, which was contrary to what Datta and Gottenberg [20], Lemaitre [22] and Lighthill [28] had found. This

discrepancy was re-examined by Lucey and Carpenter [29] from a theoretical standpoint, and revealed to have stemmed from the assumptions Shayo had made to simplify the calculations. Further, Eloy and Souillez [30] performed an analytical study with no limiting assumptions and showed that the system is in fact more stable for smaller plate spans; a statement consistent with the results of Argentina and Mahadevan [25].

Although linear Euler-Bernoulli model is proven accurate for studying the critical velocity, it is not capable of describing the behaviour of the structure after flutter happens. This is because the large deflections associated with flutter render the behaviour highly nonlinear. Hence, Tang et al. [31] accounted for the nonlinearity by adding a condition of inextensibility to the beam, and used numerical vortex lattice model [21] to calculate the aerodynamic forces. Their work was theoretically extended by Attar et al. [32] to include nonlinearities in the vortex lattice model as well. Further, Tang and Païdoussis [33] introduced material damping of the Kelvin-Voigt type [34] to the nonlinear model.

A general understanding on flutter, stability analysis and modeling approaches is made possible through an early monograph published by Dowell [35]. Later, Païdoussis [36] summarized the flow-induced vibrations and instabilities, providing a more in-depth understanding of the various problems in as well as covering different areas of the subject.

Contribution

The goal of this project is to develop a novel energy harvesting solution, where the mechanical energy of a fluttering cantilever is converted to electrical energy by means of a piezoelectric transducer. A low-cost Polyvinylidene Fluoride (PVDF) film sensor, which is often used as strain gauges and contact microphones for vibration or impact detection, is used as the energy harvester. These sensors are constructed of a layer of PVDF film, sandwiched between two electrodes meant for picking up the electric charge

the film produces under mechanical stress. When immersed in a wind flow of adequate speed, a cantilevered PVDF sensor will flutter and thus generate a varying charge distribution in the PVDF film. If the electrodes are connected to an electrical load, the variations in the charge distribution cause an alternating current in the circuit. The properties of the current depend on various parameters such as the vibration frequency and amplitude, and the electromechanical conversion characteristics of the PVDF film.

The first step towards realizing our concept of flutter-based energy harvester is to understand the physical nature of flutter, as well as piezoelectric materials. Therefore an extensive literature review is conducted on fluid-structure interactions and piezoelectric energy harvesting. The theoretical basis provided by this study resulted in a mathematical model of the system, capable of determining the critical velocity, fluttering characteristics of the PVDF patch and the output voltage. A set of experiments was then designed based on the critical velocity predicted by the math, to verify the energy harvesting capacity of the proposed design.

The output power of the energy harvester was measured for various load resistances, using a data acquisition method specific to the needs of our experiment, and the optimal load resistance and the maximum attainable harvesting capacity was determined. Although the experiments validated the critical velocity and the frequency response calculated by the model, the flutter of the PVDF sensor was drastically stronger than the expected magnitude. This discrepancy along with the main focus of this project to propose a new energy harvester concept, called for an alternative approach for assessment and correction of the theoretical results based on empirical methods. These techniques were able to reproduce the experimental data.

Finally, inspired by the great potentials of the empirical methods a novel video vibrometry system was designed for measuring large deflection vibrations. Using a high-speed video camera, the fluttering PVDF was filmed and the picture was analyzed by means of an innovative algorithm to measure the frequency and the magnitude of the vibration. The results were also

combined with the empirically identified piezoelectric characteristics of the PVDF film sensor to estimate the output voltage of the system. These calculations lead to an improved accuracy in determination of the output power, while creating an alternative measurement technique for application where laser vibrometry is not possible.

Thesis Outline

Chapter 2 explains the theory of flutter in flexible structures, and derives the mathematical model of the energy harvester by considering piezoelectric properties for the vibrating structure. The first phase of experiments and the result comparison is covered in Chapter 2 as well. In Chapter 3, the experimental approach for measurement of the energy harvesting capacity of the system is presented. The results of this study are compared to the findings of Chapter 2 in order to verify the theoretical data. Also the errors in determination of flutter dynamics and electromechanical conversion is discussed, and corrections are made in order to improve the theoretical results. Inspired by these empirical corrections, Chapter 4 discusses an innovative technique as an alternative to laser vibrometry in case of high deflection vibrations. Finally, the conclusive remarks and the future directions of this work are covered in the 5^{th} Chapter.

Chapter 2:

Theoretical Approach to Piezoelectric Energy Harvesting From Flutter

In order to design a flutter-based piezoelectric energy harvester we must first understand the nature of flutter and the parameters that contribute to it. This knowledge will be essential for studying the feasibility of flutter power harvesting, demonstrating the power generation potential and identifying the key design parameters. In this chapter, we first create a general understanding of flutter by presenting the linear model. This model is then used as the basis for the theoretical analysis. The effect of electromechanical transduction is also discussed by introducing the piezoelectric effect into the equations. To run the simulations using the linear model, the physical properties of the PVDF beam are first measured by experimental system identification. These properties are used in the solution of the linear model and the results are presented and discussed. Due to the shortcoming of the linear model, an improvement is sought by means of considering the large deformations that create a nonlinear vibration. The results of this simulation method are presented at the end of this chapter.

Linear Modeling of Flutter

Figure 1 illustrates the simplest fluid-structure configuration leading to occurrence of flutter, where a cantilever beam is subjected to a laminar wind flow. The schematic in Figure 1 is used to derive a mathematical model of flutter and discuss the various aspects of this phenomenon.

Figure 1: Schematic of a Fluttering Cantilever

Based on the Euler-Bernoulli linear model, the differential equation associated with the system in Figure 1 is of the form [35]:

$$EIw'''' + \rho_s A\, \ddot{w} + \Delta p = 0 \tag{1}$$

In Equation(1) spatial and temporal differentiation is shown by prime and dot, respectively. w is the transverse deflection of the beam (Figure 2), which is a function of both location on the beam and time. The other parameters in Equation(1) are the beam's density (ρ_s) cross-sectional area A, flexural rigidity (EI) and the fluid load (Δp).

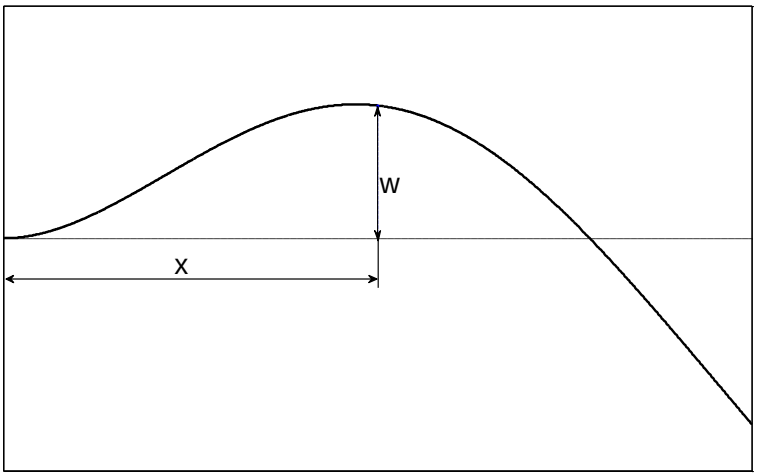

Figure 2: Typical Beam Deflection

Several methods could be used to determine the value of Δp including Slender Wing Theory [21], Theodorsen's Theory [24], Vortex Lattice Method [37], etc. Each of these methods provides a degree of accuracy while each has its own shortcomings in terms of complication and computation intensity.

Our application is energy harvesting from a regular fluid flow that can be found in the surroundings of typical industrial applications, Therefore the flow can usually be assumed inviscid, incompressible and laminar. Here, we follow the approach of Lemaitre et al. [22] which uses the slender-wing theory for its validity within the conditions of engineering non-aviation problems. According to Slender Wing Theory, the pressure forcing due to the fluid flow can be calculated as [20]:

$$\Delta p = M_f U^2 \frac{\partial^2 w}{\partial x^2} + 2M_f U \frac{\partial^2 w}{\partial x \partial t} + M_f \frac{\partial^2 w}{\partial t^2} \quad (2)$$

In Equation(2), U and M_f are the flow velocity and the fluid-added mass, respectively. The fluid added-mass depends on the geometry of the surface of the plate and for a flexible beam it is $M_f = \pi \rho_f b^2/4$ [22] with ρ_f and b being the fluid density and the beam's width, respectively. Each term in Equation(2) represents a different influence of the flow on the vibrating beam. The first term is the centrifugal force due to the flow of the fluid over the curved parts of the beam. The second term is a Coriolis force since each of the beam's infinitesimal parts are somewhat rotating relative to the flow which has a linear velocity. Finally the last term is the inertial term due to the motion of fluid particles along with the transverse deflection of the cantilever beam.

As inferred by Equation(2), fluid forces are dependent upon the value of the flow velocity U. Below a certain fluid velocity, called the critical velocity, the forcing terms are not strong enough to overcome the flexural rigidity and the inertia of the beam to start the vibrations. In fact, these forcing terms help stabilize the system so that every oscillation induced by an initial condition or forcing fluctuations will be damped by these forces. As the flow velocity is increased towards and beyond the critical value U_c, the influence of these terms becomes significant and the damping of the system becomes negative, thus resulting in instability of the system.

The first step in analyzing flutter is to determine the critical velocity. Once this property of the system is found, further investigation can be performed on the post-flutter behaviour of the beam.

Solution Method

Calculating the critical velocity is possible via solving the partial differential equation of motion for the transverse deflection. The candidate solution of any second order differential equation is in exponential form of $Ae^{j\omega t}$, with a complex angular frequency ω. The imaginary and real parts of the solution determine the oscillation frequency and the damping of the system, respectively. Hence, the critical velocity is the value of flow velocity at which the damping of the system becomes negative.

Due to the complexity of the differential equations associated with flutter, analytical solution would be very complicated and beyond the scope of this thesis. Moreover, there exist no exact solutions for the case of nonlinear differential equations. Approximate numerical methods, on the other hand, take advantage of the highly-developed processing powers of modern computers, while maintaining acceptable accuracy. The most common technique is to decompose the transverse deflection of the beam into spatial and temporal components, as demonstrated in Equation(3). This method is known as Galerkin's decomposition method.

$$w(x,t) = \sum_{m=1}^{\infty} \psi_m(x) \cdot q_m(t) \tag{3}$$

Here, the spatial functions, $\psi_m(x)$ are the shape functions that must satisfy the boundary conditions of the physical problem, and the temporal functions $q_m(t)$ are *generalized coordinates* determining the participation weight of each of the shape functions. Galerkin's method is similar to the well-known separation of variables technique in solving partial differential equations. The difference, however, is that the spatial and temporal functions are both solved

for in the latter, while in the former, the spatial functions are assumed beforehand. The decomposition then reduces the partial differential equation to a set of ordinary differential equations, with the temporal functions remaining as the unknowns.

Any set of functions that satisfy the boundary conditions of the differential equation can be chosen as shape functions. Nevertheless, it is common practice (and quite convenient) to consider the *in vacuo* mode shapes of the cantilever beam, since they are easily calculable and meet the boundary conditions. These mode shapes are the eigenfunctions of the Euler-Bernoulli beam equation without considering the fluid effects. To solve these in vacuo differential equations, we can use separation of variables. Without the pressure term in Equation(1), it can be solved as follows:

$$\left.\begin{matrix} EIw''' + \rho_s A w = 0 \\ w(x,t) = \psi(x)q(t) \end{matrix}\right\} \Rightarrow EI\psi''''q + \rho_s A\psi\ddot{q} = 0$$

$$\Rightarrow \frac{\psi''''}{\psi} = -\frac{\rho_s A}{EI}\frac{\ddot{q}}{q} = \beta_n^4$$

Where β_n is a constant because ψ and q are functions of x and t, respectively, and thus no general equality can exist between functions of ψ and q unless both sides of the equality are constant. Therefore a set of trigonometric differential equations is derived from the above equality:

$$\begin{cases} \psi'''' - \beta_n^4\psi = 0 \\ \ddot{q} + \dfrac{EI}{\rho_s A}\beta_n^4 q = 0 \end{cases}$$

These equations represent the temporal and spatial components of the in vacuo vibration of the beam. Solving the first equation results in the mode shapes of the beam, each corresponding to a frequency determined by solution of the second equation. Solving the spatial equation for ψ_n yields:

$$\psi_n = A\sin\beta_n x + B\cos\beta_n x + C\sinh\beta_n x + D\cosh\beta_n x \quad (4)$$

In order to determine the coefficients of each of the trigonometric functions in Equation(4), we need to apply the boundary conditions of the cantilever beam:

- Zero deflection and slope at the clamped end: $\psi(0) = \psi'(0) = 0$
- Zero moment and shear force at the free end: $\psi''(l) = \psi'''(l) = 0$

By considering these conditions, Equation(4) can be rewritten as:

$$\psi_n = \cosh\beta_n x - \cos\beta_n x + \sigma_n(\sinh\beta_n x - \sin\beta_n x) \quad (5)$$

Equation(5) shows the definition of the beam's in vacuo mode shapes. The parameters of this equation are also found by applying the boundary conditions as:

$$\cos\beta l \cdot \cosh\beta l = -1 \quad (6)$$

$$\sigma_n = \frac{\sin\beta_n l - \sinh\beta_n l}{\cos\beta_n l + \cosh\beta_n l} \quad (7)$$

These mode shapes are mutually orthogonal meaning that:

$$\int_0^l \psi_m \psi_n = 0 : m \neq n \quad (8)$$

Now that the shape functions of Galerkin's expansion are known, the transverse deflection of the beam can be written in terms of the mode shapes and generalized coordinates. Prior to this step, however, we must determine the number of modes we need for our approximation, since infinite number of β_n values can be calculated from Equation(6), each yielding a different mode shape of the vibration. The number of the required modes depends on the

problem and the proper level of accuracy. Since more accuracy is attainable by using a higher number of modes, we can iteratively raise the number of modes until the solution reaches a plateau with an acceptable variation.

Substituting Galerkin's expansion in Equation(1) decomposes the equation into spatial and temporal terms. Moreover, in order to convert the partial differential equations to a set of ordinary differential equations, we can take advantage of the orthogonality of the mode shapes. In this procedure the equation resulting from substitution of Equation(3) into the Euler-Bernoulli equation is multiplied by ψ_n and then integrated over the length of the beam. This leads to a set of N ordinary temporal differential equations of the form:

$$m_{nn}\ddot{q}_n + \sum_{m=1}^{N}[c_{nm}\dot{q}_m + k_{nm}q_m] = 0 : n = 1, \cdots, N \tag{9}$$

Where:

$$m_{nn} = \left(M_f + \rho_s A\right)\int_0^l \psi_n^2 dx$$

$$c_{nm} = 2M_f U\int_0^l \psi_n \psi_m' dx$$

$$k_{nm} = EI\int_0^l \psi_n \psi_m'''' dx + M_f U^2 \int_0^l \psi_n \psi_m'' dx$$

Equation(9) can be used to solve for the generalized coordinates of the system. These equations define an N-mode system and the general solution of this type of equations is:

$$q_n = A_n e^{j\omega_n t} \tag{10}$$

Each mode has a complex frequency of ω_n. The occurrence of flutter is because the real part of one of these frequencies becomes negative. The other modes have positive damping and do not contribute to steady-state vibrations. Once the mechanical parameters of the problem such as the

density and flexural rigidity of the beam are known, we can proceed to calculating the critical velocity of flutter.

Piezoelectric Energy Harvesting

The next modeling step is to include the piezoelectricity of the fluttering beam. Piezoelectric sensors and energy harvesters vary in their forms and configurations. Figure 3 shows a unimorph PVDF film sensor, where a single layer of the polymer is mounted on a substrate of flexible material. Another common type of these transducers is bimorph PZT sensors that consist two layers of piezoelectric ceramics mounted on a substrate material. The flexibility required by our application dictates a lightweight and compliant patch, therefore PVDF film sensors are often designed in unimorph configurations, including a flexible Mylar substrate (Figure 3).

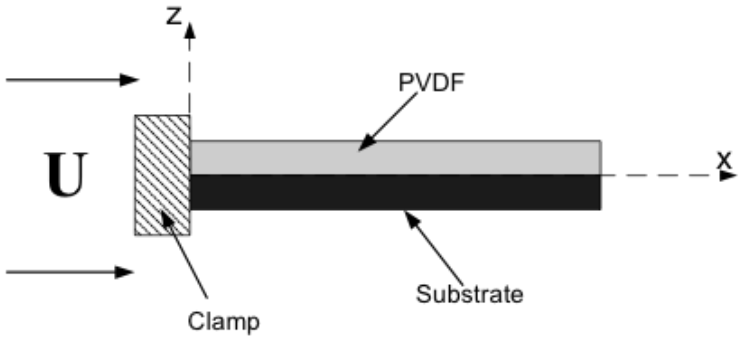

Figure 3: Schematic of the Energy Harvester Patch

The PVDF converts the mechanical deformations into a voltage difference, which is collected by a couple of electrodes attached to either faces of the PVDF film. To evaluate the produced power, we should first consider the piezoelectric constitutional relations. These relations specify the coupling between the strain and the electric field. The fundamental equation for piezoelectric material is [38]:

$$D_3 = d_{31} T_1^p + \varepsilon_{33}^T E_3 \tag{11}$$

Where D_3, d_{31} and ε_{33}^T are the electric displacement, piezoelectric effect and the permittivity at constant stress, and T_1^p and E_3 are the axial stress in the piezoelectric film and the voltage magnitude of electric field, respectively. Using $\varepsilon_{33}^S = \varepsilon_{33}^T - d_{31}^2 Y_p$, that relates permittivity at constant strain to permittivity at constant stress based on the Young Modulus of the piezo layer (Y_p), Equation(11) can be rewritten as:

$$D_3(x,t) = d_{31} Y_p S_1(x,t) - \varepsilon_{33}^S \frac{v(t)}{h_p}$$

Considering $S_1(x,t) = -c(\partial^2 w/\partial x^2)$ where c is the maximum distance from the beam's neutral axis ($c = h_p/2$), and:

$$i(t) = \frac{dq}{dt} = \frac{d}{dt}\int \boldsymbol{D} \cdot \boldsymbol{n} dA$$

The equation for the produced current is:

$$i(t) = -\int_0^L d_{31} Y_p h_{pc} b \frac{\partial^3 w}{\partial x^2 \partial t} dx - \frac{\varepsilon_{33}^S bL}{h_p} \frac{dv}{dt} \qquad (12)$$

It is common in the literature to consider PVDF both as a voltage or current source and interchanging between the two configurations is possible through Thevenin-Norton equivalencies [1]. The film sensor is connected to a circuit with the load resistance R_L as shown in Figure 4. Note that in this study, the internal capacitance of the PVDF ($C_p = \varepsilon_{33} bL/h_p$) is accounted for in the equations and thus is considered encapsulated in the PVDF package. the generated voltage is:

$$v(t) = R_L \cdot i(t) \qquad (13)$$

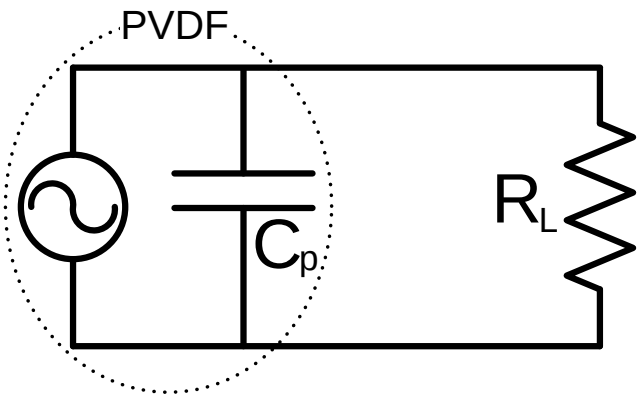

Figure 4: Schematic diagram of the Circuit

Finally, combining Equations(12) and(13), the differential equation for the produced voltage is derived as:

$$\frac{\varepsilon_{33}^{S} bL}{h_p} \cdot \frac{dv}{dt} + \frac{v(t)}{R_L} = -\int_0^L d_{31} Y_p h_{bc} b \frac{\partial^3 w}{\partial x^2 \partial t} dx = -d_{31} Y_p h_{bc} b \frac{\partial^2 w}{\partial x \partial t}\Big|_{x=0}^{L} \quad (14)$$

Equation(14) is a first-order linear differential equation and can be used to calculate the output voltage of the energy harvesting system, once the mechanical deformations of the beam are found. A number of points can be implied from this equation:

Importance of Vibration Frequency: Since a time derivative of the transverse deflection of the beam is present in the right-hand side of the equation, vibrations with small tip deflection but high frequency can theoretically produce voltages comparable to ones with large displacements and low frequencies.

Effect of the Load Resistance: By changing the load resistance, the generated voltage of the system can be changed. If we assume Equation(15) in a general form with R_L left as the only parameter:

$$A\dot{v} + \frac{v}{R_L} = f(t) \tag{15}$$

We can use Laplace transform to get an idea as to how the amplitude of the output voltage changes with different values of the load resistance. Since flutter vibrations have constant amplitude and frequency, the Laplace transform of the excitation part in Equation(15) can be considered constant:

$$V\left(sA + \frac{1}{R_L}\right) = F \Rightarrow V = F \cdot \frac{R_L}{1 + sAR_L}$$

This equation requires the output voltage to react to changes of the load resistance in the form presented in Figure 5.

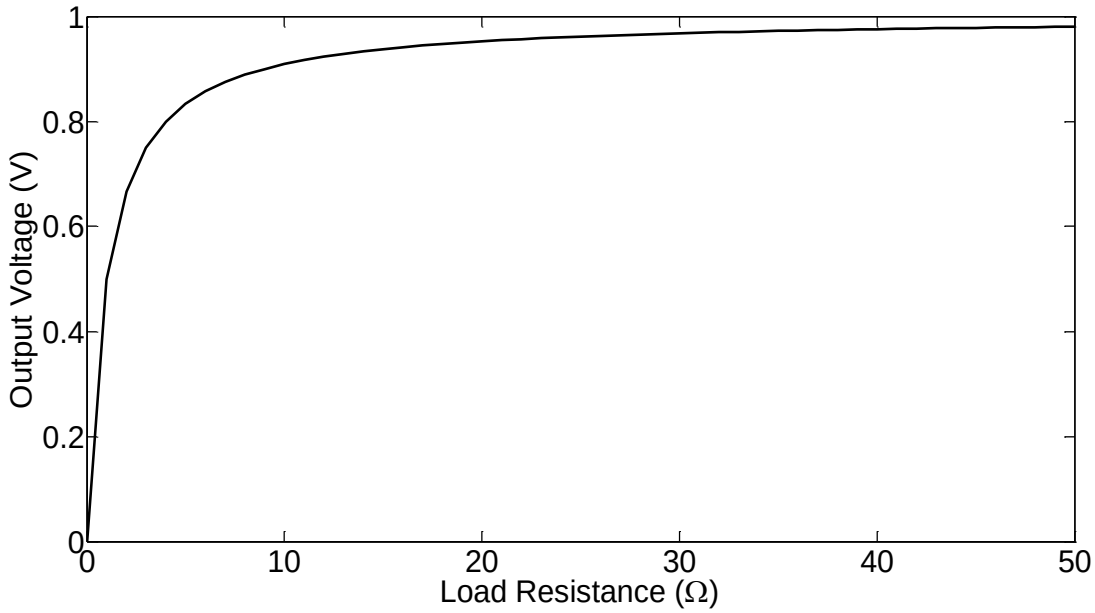

Figure 5: Schematic Changes in Voltage versus R values

In this figure, to show the general trend, all parameters other than R_L and V are considered unit. On the other hand, since the output power of the system is calculated by $P = \frac{V^2}{R}$, the output power should have a peak at a certain value of load resistance, which is schematically shown in Figure 6:

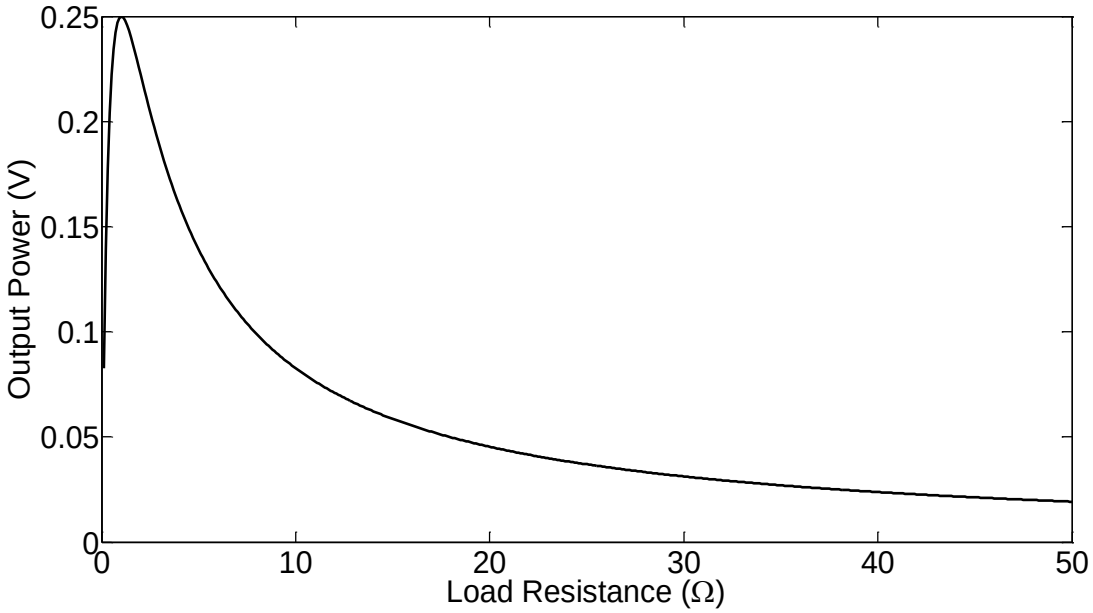

Figure 6: Schematic Changes in Power versus R values

This peak corresponds to an *optimum load* where the output power of the system is maximized. The location of 3the point is determined impedance matching between the load resistance and the PVDF.

Backward Coupling

The mechanical and electrical behaviours of the piezoelectric transducer are coupled in a way that the produced voltage introduces a tension, subsequently, and inflicts a bending moment into the composite strip. This effect is known as *backward coupling*. To introduce the piezoelectricity to the equations, the stiffness term of Equation(1) can be expressed for the bending moment of the beam as:

$$EI\frac{\partial^2 M_p}{\partial x^2}$$

Where M_p is the bending moment throughout the composite beam. If the width of the PVDF is denoted as b, this bending moment can be calculated:

$$M_p = -\int_{h_b}^{h_c} T_1 b y dy$$

In this equation, h_b and h_c are the distances of bottom and top layers of the piezoelectric film from the neutral axis, respectively. The electric field and tension are related as [38]:

$$T_1 = Y_p(S_1^p - d_{31}E_3) \tag{16}$$

Now considering the fact that $E_3 = -v(t)/h_p$ is relating the electric field to the voltage (v) and the thickness of the PVDF layer, since the mechanical strain is a function of the beam's radius of curvature, the total bending moment within the piezoelectric layer will be:

$$M_p = Y_p I \frac{\partial^2}{\partial x^2} - \vartheta v : \vartheta = \frac{Y_p d_{31} b}{2h_p}(h_c^2 - h_b^2)$$

This added moment $(-\vartheta v)$ is applied on the part of the beam to which the electrodes are attached. If electrodes are placed between x_1 and x_2 along the length of the beam, $H(x - x_1) - H(x - x_2)$ should be multiplied by the voltage effect term, where $H(x)$ is the Heaviside step function [39]. Here, it is considered that the electrodes cover the whole beam thus the added moment becomes:

$$M_p = Y_p I \frac{\partial^2}{\partial x^2} - \vartheta v[H(x) - H(x - L)]$$

The first term is bundled within the first term in Equation(1), and the second term, when twice differentiated with respect to x, adds a forcing term:

$$EI\frac{\partial^4 w}{\partial x^4} + M_f U^2 \frac{\partial^2 w}{\partial x^2} + 2M_f U \frac{\partial^2 w}{\partial x \partial t} + \left(\rho_s A + M_f\right)\frac{\partial^2 w}{\partial t^2} - \vartheta v\left[\frac{d\delta(x)}{dx} - \frac{d\delta(x-L)}{dx}\right] = 0$$

Where $\delta(x)$ is the Dirac delta function. The added forcing tem changes the dynamics of the system based on the output voltage of the PVDF, coupling the equations of motion and voltage generation.

PVDF Patch System Identification

Although electrical and mechanical properties of PVDF are accessible in the literature, since the patch being used for this study is meant for commercial rather than research purposes, no information on structural details of the film sensor is available. However, it is necessary that certain specifications are determined so the beam can be modeled with acceptable accuracy. Therefore the mechanical properties of the path, including flexural rigidity, mass per unit length and structural damping, are evaluated through a system identification procedure.

Mass per unit length of the PVDF beam is easily measurable by means of a scale. To this end, a $27.88 \pm 0.01\, mm$ piece of the PVDF patch was cut and found to weigh. $0.14 \pm 0.01\, gr$. Therefore the mass per unit length of the beam is $\rho_s A = 0.005 + 0.0004\, kg/m$. In order to determine the flexural rigidity, however, a proper method is needed since the high compliance of the patch makes it inaccurate to simply observe the tip deflection caused by a certain tip-mass and calculate the stiffness.

Based on the Galerkin's decomposition of the in vacuo differential equation, Equation(17) is derived for calculating the natural frequencies of the beam based on the flexural rigidity and the mass-per-unit-length of the beam. Hence, if the frequencies are known, the unknown stiffness can be derived from this equation.

$$\omega_n = \beta_n^2 \sqrt{\frac{EI}{\rho_s A}} \tag{17}$$

The natural frequencies of the cantilever beam can be measured with an experiment, where the base of the beam is mounted on a shaker head and is excited by a range of frequencies. Fully clamped boundary condition is maintained by gluing the PVDF film to a Plexiglas fixture, which is bolted to the shaker head (Figure 7).

Figure 7: PVDF Mounted on the Shaker Head

The response of the beam as the deflection of the tip is measured using a Polytec PSV-400 Scanning Vibrometer. Equipped by a video camera and a scanning laser, this measurement device provides a video image of the object to be analyzed. The point of vibrometry can be located using a computer mouse. The tip velocity is then graphed versus the excitation frequency which is input from the shaker controller. When the frequency sweep of the shaker coincides with the natural frequencies of the beam, a peak in the response curve is observed due to resonance. Figure 8 shows the experiment result for excitation frequencies of 5-100 Hz.

The two peaks visible in Figure 8 correspond to the frequencies of the first two natural vibration modes of the beam. Nonetheless, these frequencies are the *damped natural frequencies* of the beam. The system is damped by both the material damping and the ambient air, which affects the observed resonance frequency:

$$\omega_d = \omega_n\sqrt{1-\zeta^2}$$

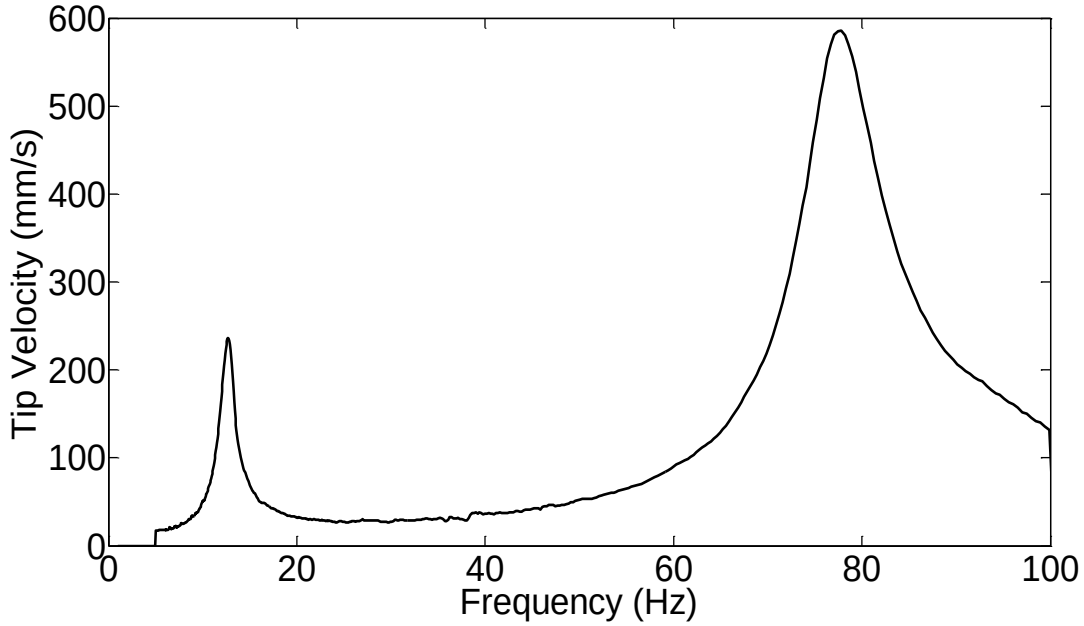

Figure 8: Tip Velocity data from the Shaker Experiment

ω_d is the damped natural frequency. Since the damping coefficient (ζ) is different for each of the vibration modes, the measurements have to be corrected so that the undamped natural frequency can be calculated. The empirical method for estimating the damping coefficient is to find the peak value for each mode and draw a horizontal line so that it intersects with the curve at two points with velocities equal to the peak velocity divided by $\sqrt{2}$ [40]. The frequency difference of these two points is then used to approximate the damping coefficient by:

$$\zeta_i = \frac{1}{2}\frac{\Delta\omega_r}{\omega_r} \; of \; i-th \; mode$$

In Figure 9 we show this procedure for the frequency response of the tip velocity. Hence:

$$\omega_n = \begin{cases} \dfrac{12.706}{\sqrt{1-0.503}} = 14.70 \; Hz \\ \dfrac{77.813}{\sqrt{1-0.049^2}} = 78.00 \; Hz \end{cases}$$

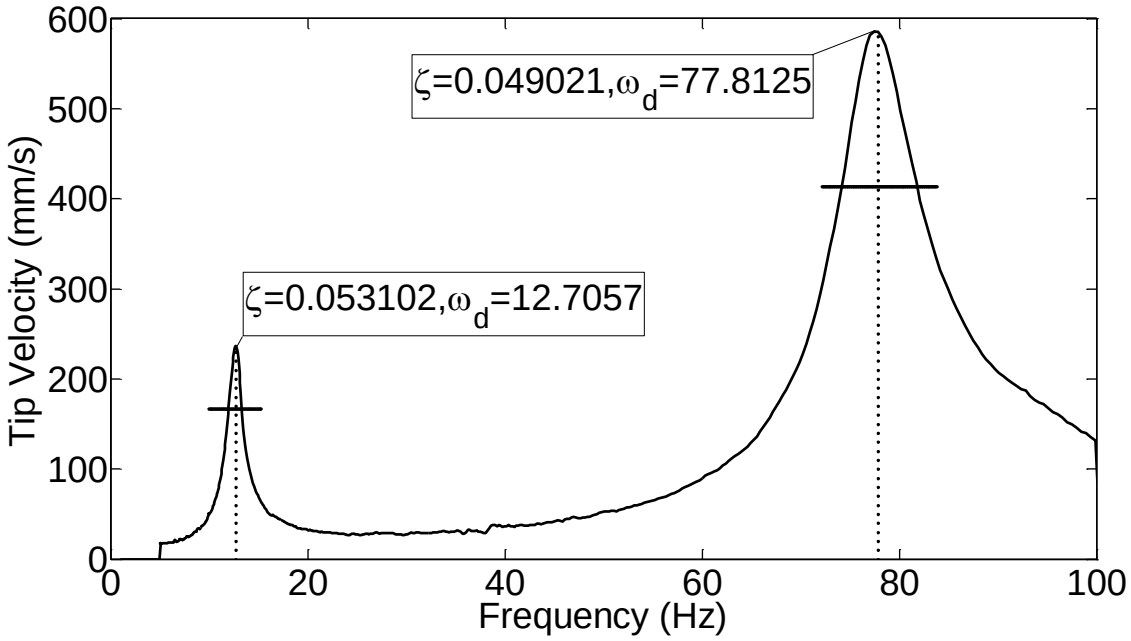

Figure 9: Approximation of the Damping Ratio

Considering the length of the beam to be $L = 63\ mm$, the flexural rigidity of the beam is calculated from Equation(17) to be:

$$EI = \frac{\omega_n^2 \cdot \rho A}{\beta^4} = 4.66 \times 10^{-5}\ \ N.m^2$$

Assessing the Significance of Backward Coupling

Although all transducers exhibit backward coupling due to their piezoelectric nature, the stress generated by this phenomenon might not be significant enough to change the movement of the system. In order to investigate whether or not backward coupling is influential in our setup, we used the shaker test to see if the vibrations of beam would be different when a load is connected to the output of the PVDF. Therefore, the same base excitation experiment is performed for the two cases of open and closed circuits and the tip deflection plotted for comparison. As it is apparent from Figure 10, the backward coupling does not change the motion of the beam significantly and can be neglected in simulations of flutter.

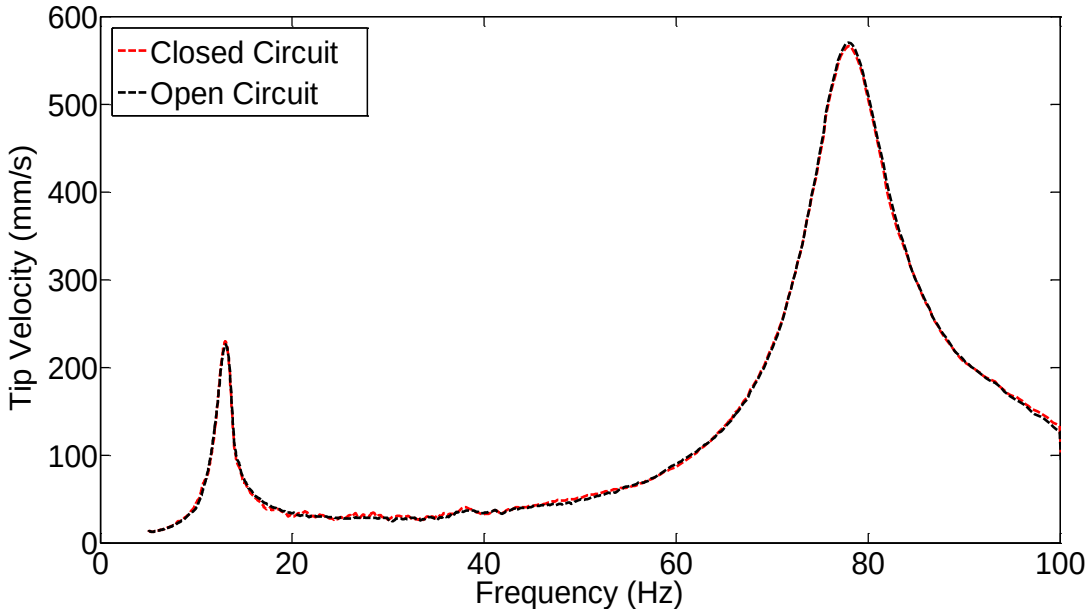

Figure 10: Tip Velocity for Open and Closed Circuit Configurations

Validity of the Linear Model

Now that we have the actual mechanical properties of the experimental setup, the temporal equations defined by Equation(9) can be used to calculate the critical velocity. As mentioned earlier, Equation(9) defines a set of N differential equations. Each of these equations results in one of the temporal functions (q_n). In order for flutter to happen, the damping of one of the vibration modes becomes negative. By substituting $q_n = A_n e^{j\omega_n t}$ in Equation(10), however, we can detect the onset of flutter by solving for the roots of the system of differential equations. When the damping of one of these roots becomes negative, the frequency of that mode grows and dominates the flutter vibration. By solving these characteristic equations we can determine the critical velocity that causes the damping to become negative. The shortcoming of this method is that due to the coupled nature of the equations, finding the characteristic equation for higher mode numbers would be a complicated task. On the other hand, we have employed the differential equation solvers available in MATLAB™. These solvers are based on state-space representation and provide the user with the tools and controls needed for approaching any type of differential equation, linear or nonlinear.

The linear model exhibits high accuracy in calculating the critical velocity. Using the results of system identification, the critical velocity of the actual system is found by a MATLAB™ code. We perform the calculation for different numbers of modes, until a plateau is reached in the result (Figure 11):

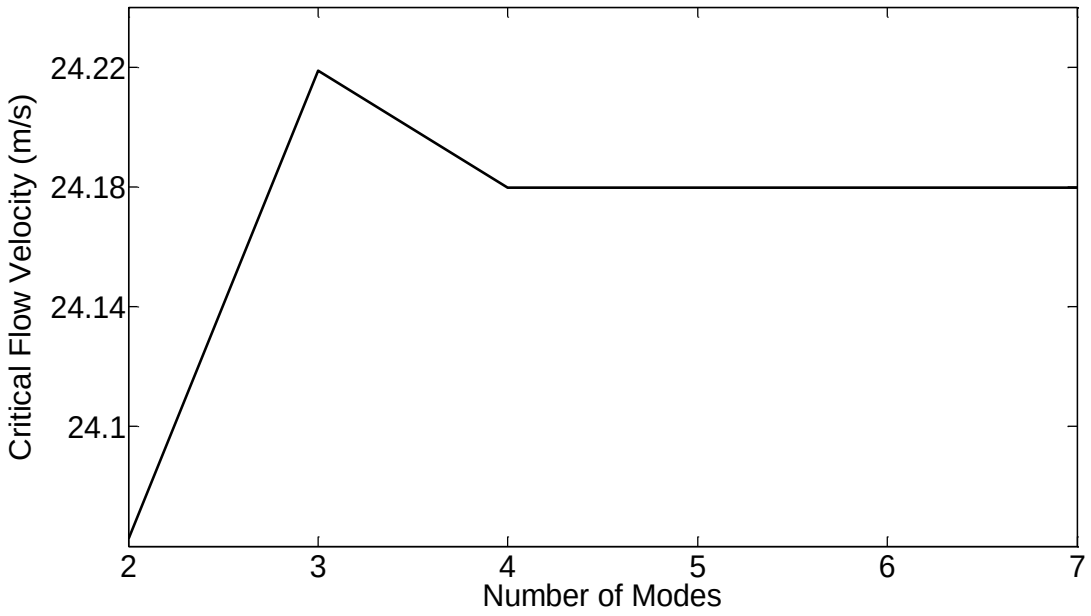

Figure 11: Calculated Critical Velocity for Different Number of Modes

The number of modes needed to approximate the critical velocity with an accuracy boundary differs for various problems. In Figure 11, four modes have been enough to achieve a stable result. For more complex or nonlinear differential equations, however, a higher number of modes are needed. The accuracy of this method is later validated by presenting actual test results. Note that in Figure 11 a minimum of modes has been used. This is because flutter cannot be observed using a single mode in Galerkin decomposition [35], which is validated by our simulations.

One assumption made by the linear model is that the deflections of the beam are of the same order as the thickness of the beam. However, flutter exerts large oscillatory forces on the beam that the linear model is no longer valid. In reality, the flutter oscillations persist with constant tip deflection amplitude. As it is illustrated in Figure 12, the linear differential equation cannot capture the finite amplitude and the solution diverges.

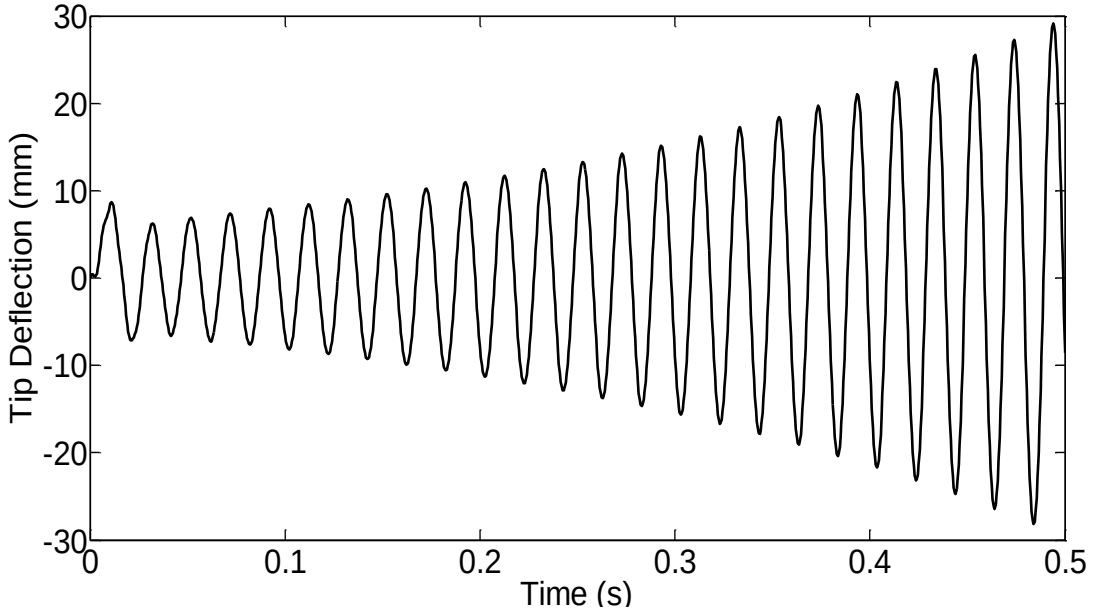

Figure 12: Divergence of the linear model

Nonlinear Flutter Analysis

As the flutter vibration amplitude grows, the axial body tensions of the beam come into play rendering the dynamics of the vibration [35]. Bending creates axial tension that in return resists bending. The longitudinal stress term is $-N_x$ where:

$$N_x = E\frac{\Delta l}{l}h \approx \frac{Eh}{2l}\int_0^l \left(\frac{\partial w}{\partial x}\right)^2 dx$$

l and h are the length and the thickness of the beam, respectively. Adding the tension term into the linear beam representation, the nonlinear equation of motion can be derived as:

$$EI\frac{\partial^4 w}{\partial x^4} - \left[\frac{Ebh}{2l}\int_0^l \left(\frac{\partial w}{\partial x}\right)^2 dx\right]\frac{\partial^2 w}{\partial x^2} + \rho_s A\frac{\partial^2 w}{\partial t^2} + \Delta p = 0$$

For the large deformations to be significant enough to influence the dynamics of the beam, the tension forces have to be of comparable magnitude as the excitation and resistance terms. By substituting this condition for the two terms of stiffness and axial tension, we can find the threshold for the

deflections to be considered large. If we assume $\partial/\partial x$ to be of the same order as $1/l$, we can compare the orders of magnitude of the stiffness term and the nonlinear tension term:

$$\left.\begin{aligned} EIw'''' &\sim \frac{Eh^3 w}{l^4} \\ N_x \frac{\partial^2 w}{\partial x^2} &\sim Eh\frac{w^3}{l^4} \end{aligned}\right\} \Rightarrow w \sim h$$

This shows that the transverse deflection of the beam has to be of the order of the beam's thickness to lead to nonlinear flutter behaviour.

By applying Galerkin's decomposition to the nonlinear equation, the MATLAB™ solvers can be used to find the temporal functions and calculate the tip deflection. The finite-amplitude oscillations of flutter are of the limit-cycle form. This means that there is a second pseudo-stability point where the amplitude of the vibration remains constant and the beam continues to vibrate.

Note that in this modeling approach, the transverse deflection of the beam is assumed to be constant along the width of the beam and therefore no tension in y-direction is considered. Also the tension model used is very simple, but it is able to capture the post-flutter finite-amplitude oscillations. More realistic and therefore complicated equations are derived and discussed in [41], [42]. Since the focus of this study is to investigate the energy harvesting capacity of the proposed concept, further complexity is avoided. Experiments will be presented to evaluate the results of this model.

Without an initial condition, these equations do not yield any results. In reality, the fluctuations in the flow initiate the instability of the system. Therefore, an initial tip velocity triggers the instability of the system. For flow velocities less than the critical velocity, the motion due to the initial condition is damped by the fluid forces and does not lead to flutter. In this simulation, a tip velocity from the order of 10^{-5} excites a rather negligible vibration is the system (Figure 13).

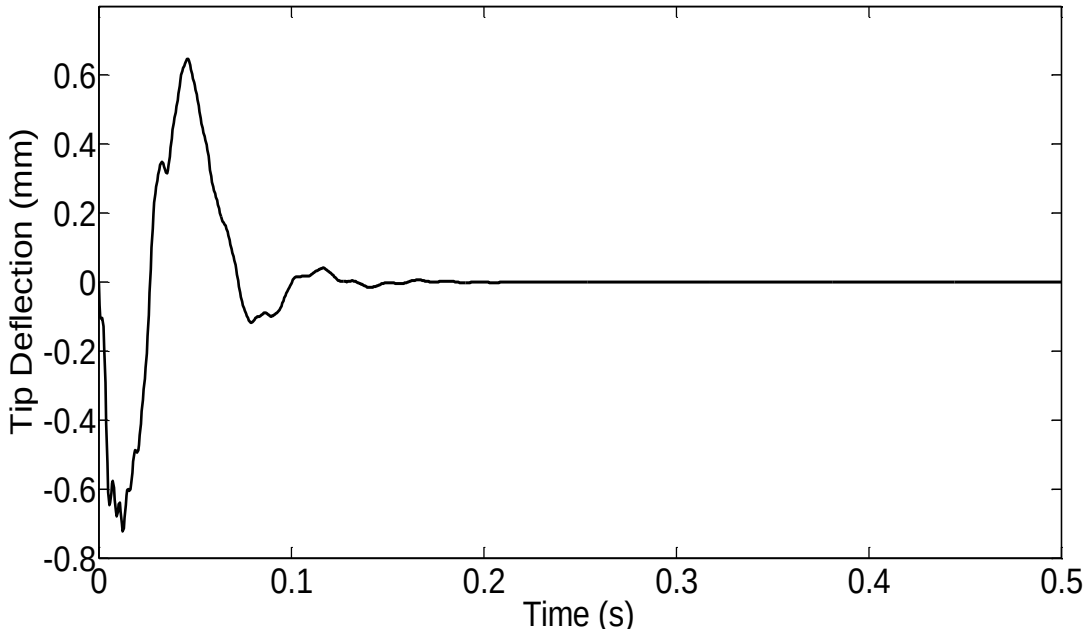

Figure 13: Tip Deflection for Flow Velocities below Critical Velocity

By increasing the magnitude of the initial condition, the system can be pushed into a temporary flutter-like phase that due to insufficient flow energy, gets eventually damped (Figure 14).

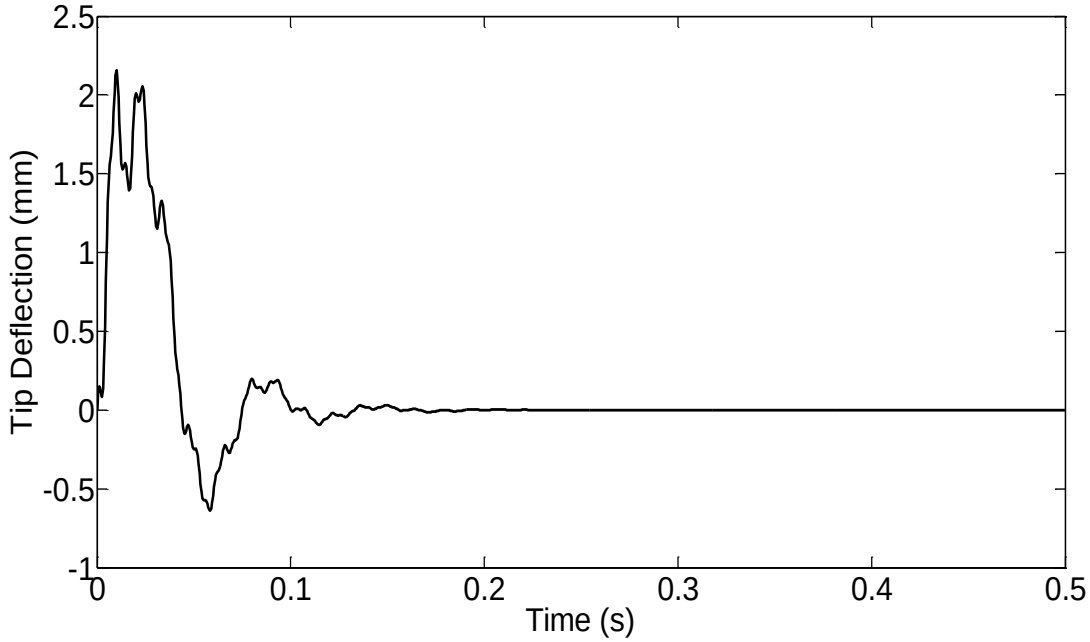

Figure 14: Tip Deflection for Large Initial Condition for $U < U_c$

For fluid velocities higher than the critical velocity, the flutter vibrations of the beam can be captured by the nonlinear model. In Figure 15 the system is subjected to a fluid velocity of $30\ m/s$ and the tip deflection is calculated. As it

can be seen in this figure, the vibration amplitude grows to a maximum and remains constant at that value. Note that the magnitude of tip deflections is comparable to the length of the beam and is two orders of magnitude greater than the thickness. This shows that the system can no longer be assumed linear.

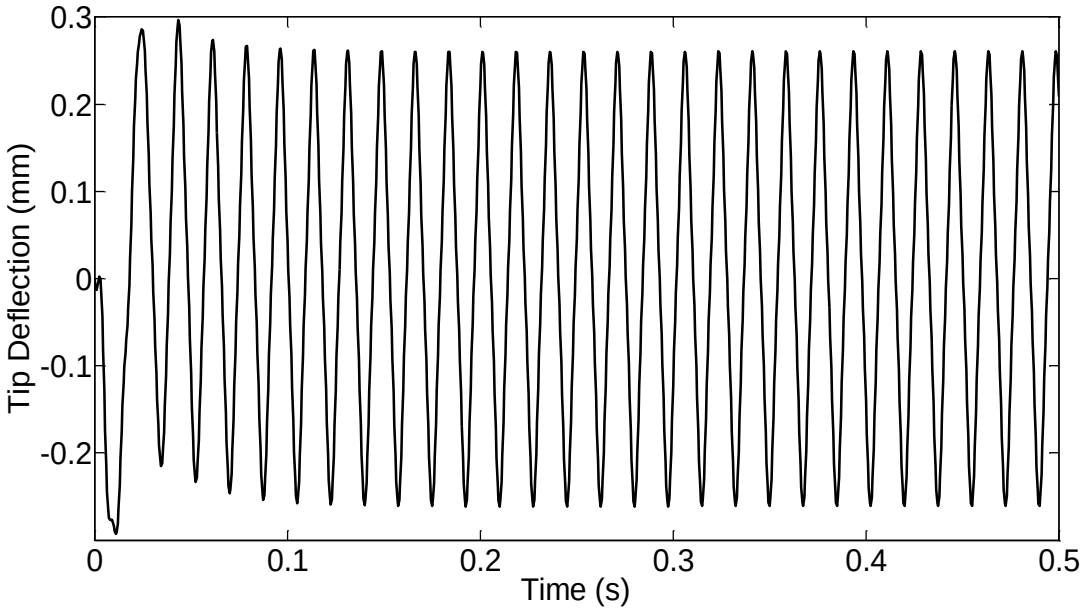

Figure 15: Simulation Results for Flutter Vibrations at $U = 30\ m/s$

The equations of the piezoelectric effect are simultaneously solved along with the equations of motion. The output voltage of the system can therefore be calculated. Figure 16 shows calculation results of solving the voltage differential equation for the load resistance of $100\ k\Omega$. The output voltage changes with the load resistance. As previously shown in Figure 5, the output voltage grows to a final value, therefore creating a peak in the power-resistance curve (Figure 6). The results of the numerical solution are in agreement with the trend anticipated by the general analytical solution. The changes of output voltage with load resistance are demonstrated in Figure 17. In this figure, the root mean square (RMS) of the output voltage approaches a final value of $9.11\ V$. The power output of the system is also calculated by $P = V^2/R$.

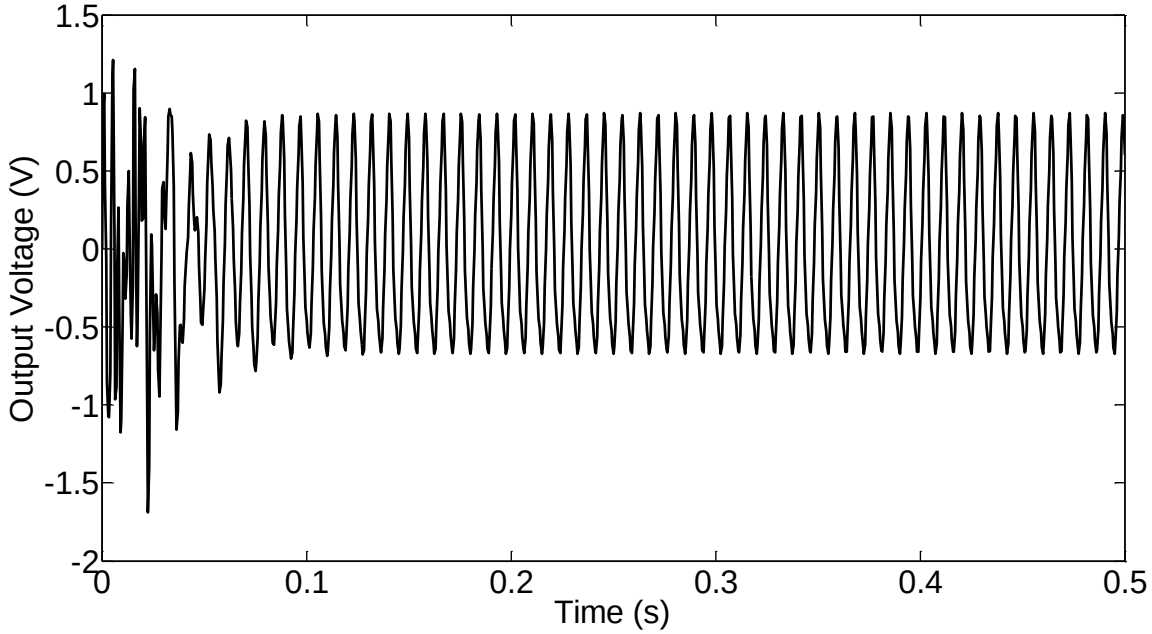

Figure 16: Simulation results for the output voltage

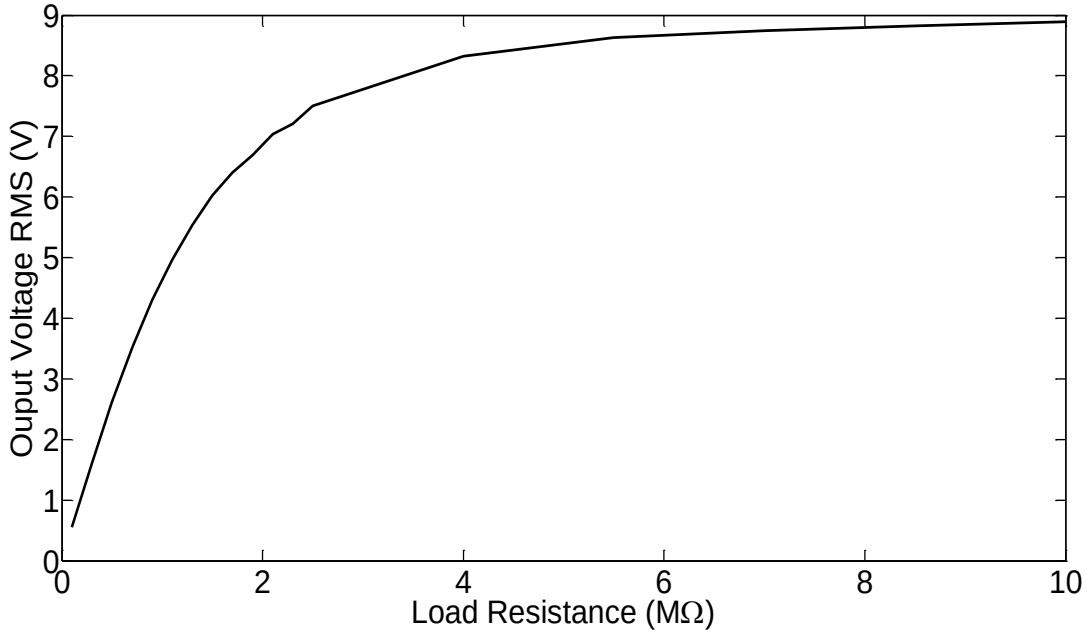

Figure 17: Changes of Output Voltage RMS with Load Resistance

As shown in Figure 18, there is a load resistance where the output power reaches a maximum of $24\ \mu W$. The optimal resistance, which depends on the material properties of the piezoelectric transducer [1], has been $1.5\ M\Omega$. The results show that the system is capable of generating enough power for remote sensor networks [43].

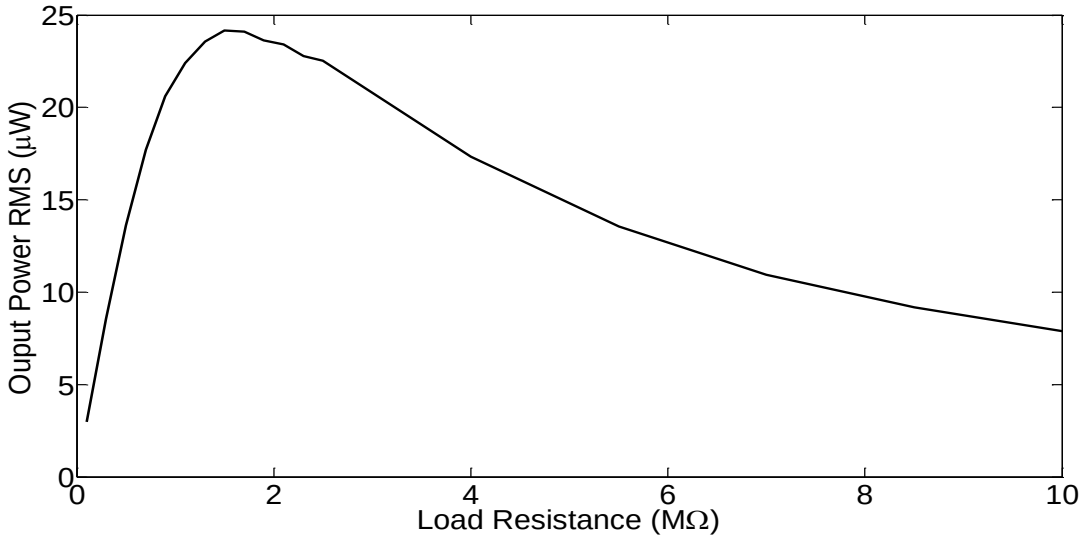

Figure 18: Changes of Output Power RMS with Load Resistance

Frequency Analysis

The frequency content of the tip deflection can be found by applying the Fast Fourier Transform (FFT) on the results presented in Figure 15.

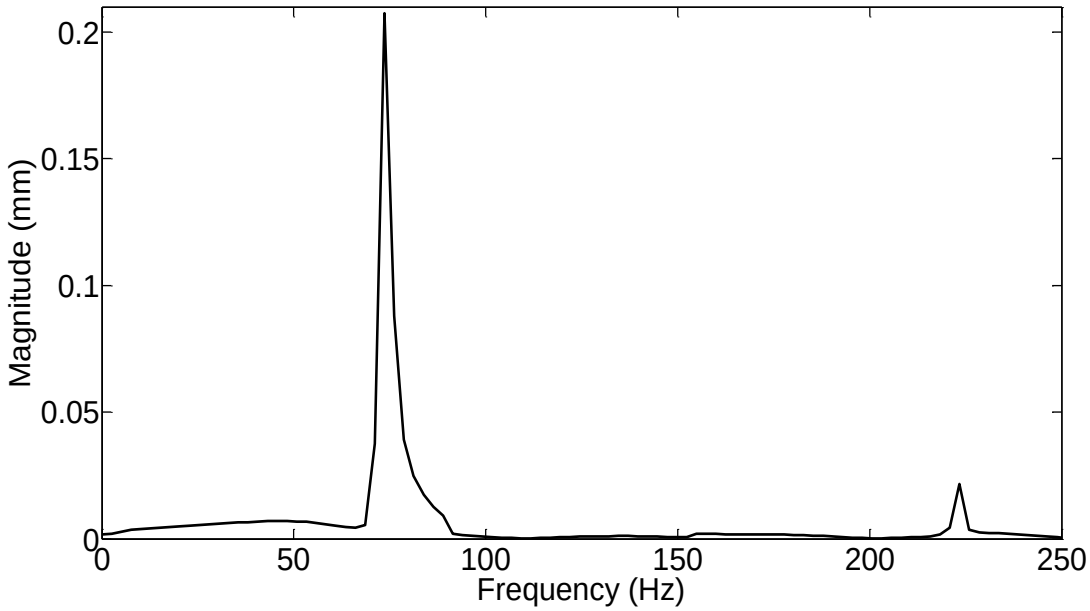

Figure 19: Frequency Content of the Tip Deflection

Figure 19 shows the frequency content of the tip deflection as calculated by the theoretical approach. In this figure, two frequencies are observed to be prominent. The number of modes assumed in Galerkin decomposition affects the number of the peaks we observe in the FFT. By changing the number of modes in the solution it was observed that the frequency content is the same

for three and four modes. For the case of two assumed modes the second peak disappears from the result, leaving only one peak in the calculated frequency content. Since there seems to be a missing peak from the frequency content, we omit the first mode from the 3-mode simulation to see if same result is obtained.

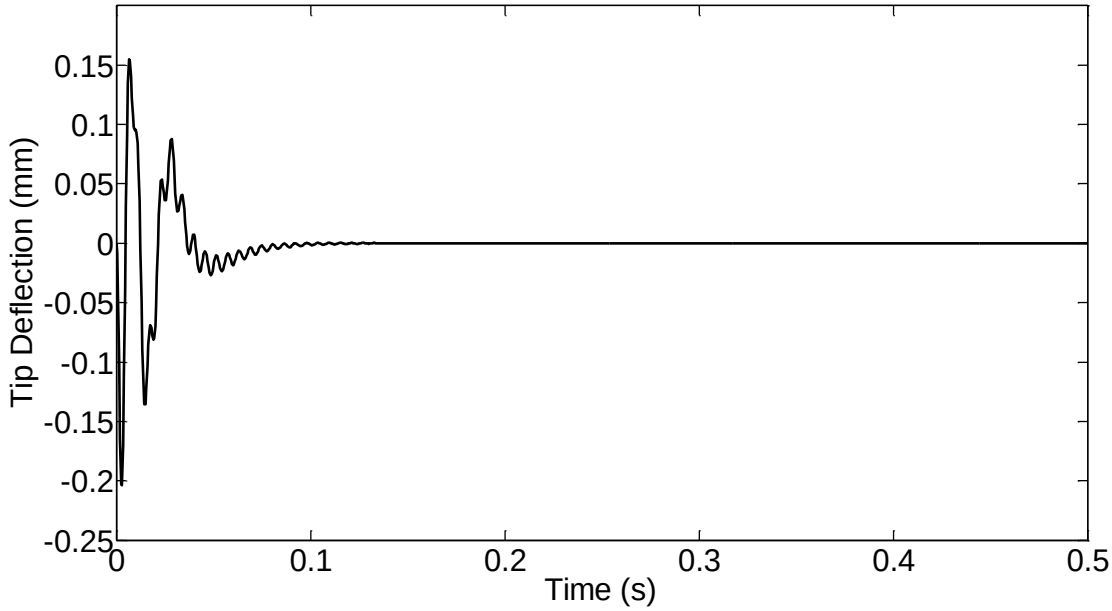

Figure 20: Tip deflection for simulation without the first mode

As it can be seen in Figure 20, flutter cannot be captured for the case where the first mode is omitted. This means that although the first mode does not appear in the frequency content of the tip deflections, it is necessary for flutter to happen. The second mode corresponds to the first peak of the frequency response, which is greater by one order of magnitude, and it is the main component of flutter vibration. That is why the time domain changes of the deflection are dominated by a single frequency and the third mode has not been significant.

The frequency content of the output voltage is also calculated using FFT. As is shown in Figure 21, the two peaks observed in the tip deflection's frequency content are present in the voltage signal at the same frequency values. By dividing the output voltage by the tip deflection, we can calculate the transfer function that converts the tip deflection (Figure 22).

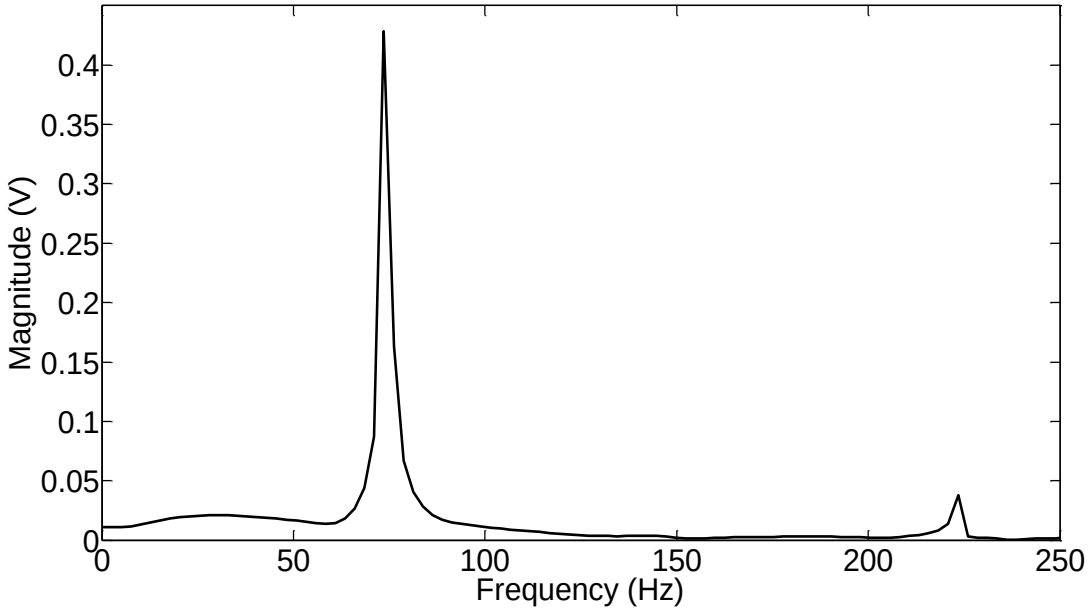

Figure 21: Frequency Content of the Output Voltage

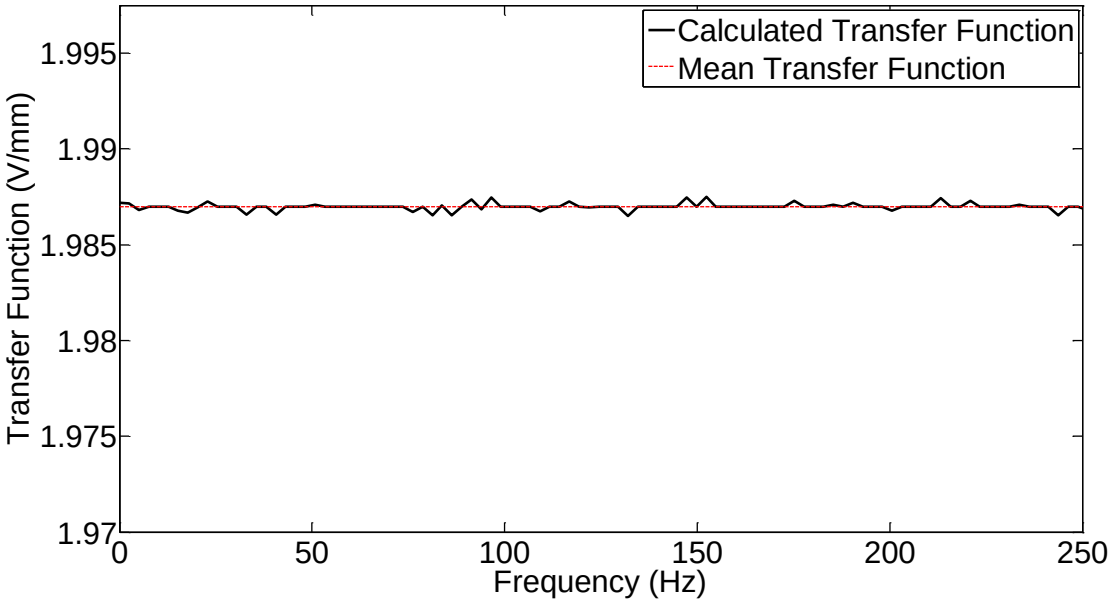

Figure 22: Theoretical Electromechanical Transfer Function

Figure 22 shows that the electromechanical transfer function of the PVDF has been virtually constant for the entire frequency range. In the next chapter, the theory is investigated through different sets of experiments, each aiming at examining a particular part of the analysis.

Chapter 3:

Experimental Approach to Piezoelectric Energy Harvesting From Flutter

In this chapter, the theoretically calculated output voltage of the piezoelectric flutter-based energy harvester is examined by experimental analysis. We first explain the wind tunnel experiment designed to asses different parts of the theoretical approach. Then the innovative data acquisition algorithm is discussed, which is created to specifically make repeatable readings of the output voltage of the wind tunnel test setup. Finally the results are presented and compared to those obtained from the theoretical approach.

Wind Tunnel Experiments

In order to validate the results of the theoretical study, as well as to determine the actual energy harvesting capacity of the proposed device, a wind tunnel experiment was designed. In this experiment, we create an environment where the output flow of the wind tunnel is used to excite the PVDF patch and cause it to flutter. Figure 23 shows the experimental setup used in this study. As it is shown in the figure, the PVDF patch is enclosed within a Plexiglas duct which is attached to the outlet of a wind tunnel. The dimensions of this duct are determined based on the calculated critical velocity obtained from the theoretical study. Also some preliminary tests were done and a qualitative knowledge on the behaviour of the vibrations was gained. The PVDF is mounted in flag-like orientation so that it cannot be bent due to its own weight. The first set of tests is conducted to investigate the role of flow velocity in the dynamics of the system. In this phase, we observe the motion of the beam for different values of flow rate in the wind tunnel. The flow rate of the wind tunnel

is adjusted by turning a knob that changes the angular frequency of the fan driving the flow.

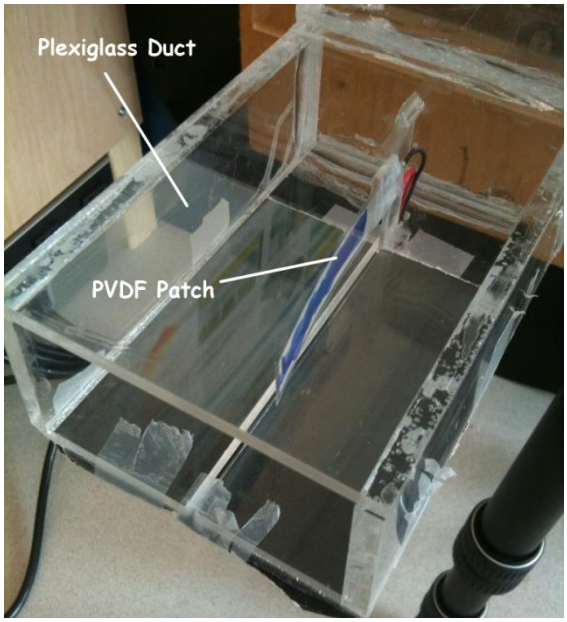

Figure 23: Experimental Setup for Investigation of PVDF Flutter

Higher flow velocities correspond to higher pressure difference between two points in the flow. Therefore, a pressure sensor is employed to measure the pressure difference between two fixed points on the wind tunnel prior to the outlet. This value is then used in a proprietary spreadsheet of the wind tunnel to calculate the flow rate and fluid velocity.

Similar to the predictions of the nonlinear model, for lower velocities, the beam is steady and any disturbance is damped. As the flow speed is raised, the disturbances become more influential and lead to temporary fluttering. At the critical velocity, however, the vibrations can start with a negligible initial excitation and fluttering will be continuous. In fact, since the flow cannot be perfectly maintained at linear conditions, the fluctuations of the flow can internally trigger the instability of the system. The flow velocity of the experimental setup is in acceptable agreement with the predicted value as resulted from the linear model. The PVDF beam lost its stability at $U = 25.15\ m/s$. The value calculated in Figure 11 is $24.18\ m/s$, which differs from the actual test data by 4%. The second step in the experimental analysis is to measure the voltage of the fluttering PVDF to validate the theoretical data. In

this regard a data acquisition method is designed to measure the output signals of the fluttering PVDF.

Data Acquisition Method for Measurement of Output Voltage

The same wind tunnel setup as Figure 23 is used for this part of the experiments and the output voltage is measured by means of a National Instruments Data Acquisition (DAQ) card. Since the load resistance experienced by the PVDF influences its output voltage and power, the internal resistance of the DAQ card ($285.4\ k\Omega$) needs to be isolated to avoid the dependency of results on measurement device.

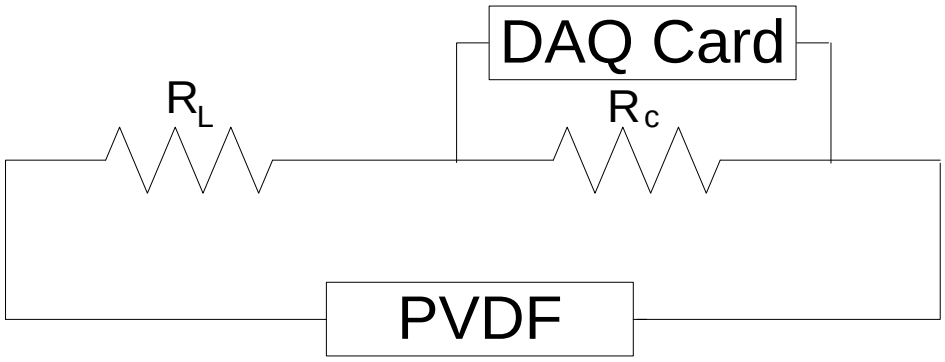

Figure 24: DAQ Circuit for Voltage Measurement of the PVDF

Therefore a characteristic resistor of $R_c = 10\ k\Omega$ is paralleled to the DAQ card so the effect of the DAQ's resistance is reduced to negligible. Figure 24 shows the circuitry used for the experiments. We use MATLAB™'s Data Acquisition Toolbox for saving and analysing the time domain voltage measured by the DAQ card. Figure 25 shows the voltage reading of the DAQ card for a load resistance of $1196\ k\Omega$. As it can be seen in this figure, due to the erratic nature of flutter, as well as the imperfections of the experimental setup to maintain a laminar wake-free flow, the raw output voltage of the PVDF is not very suitable for a repeatable reading to be possible (Figure 25). Sudden jumps and slightly varying amplitude is observed in the alternating output voltage. For longer sampling times, however, the voltage amplitude seems to have a mean value subject to temporary changes (Figure 26). Therefore, we designed a data acquisition program in MATLAB™ to read that data from the DAQ card and calculate the RMS of the voltage signal every second.

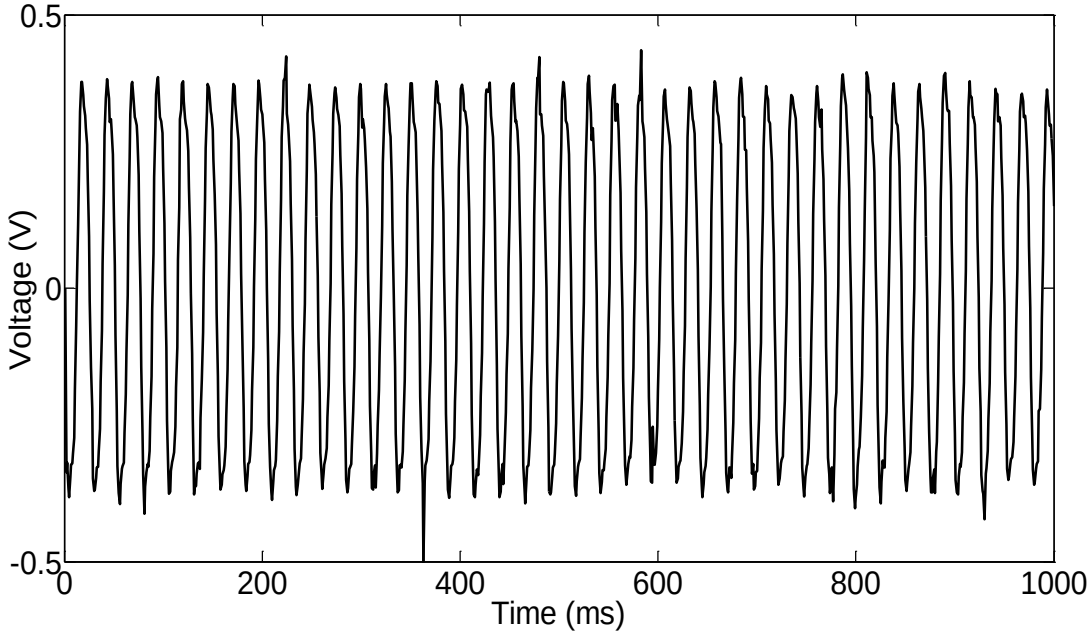

Figure 25: Time Domain Output Voltage Data

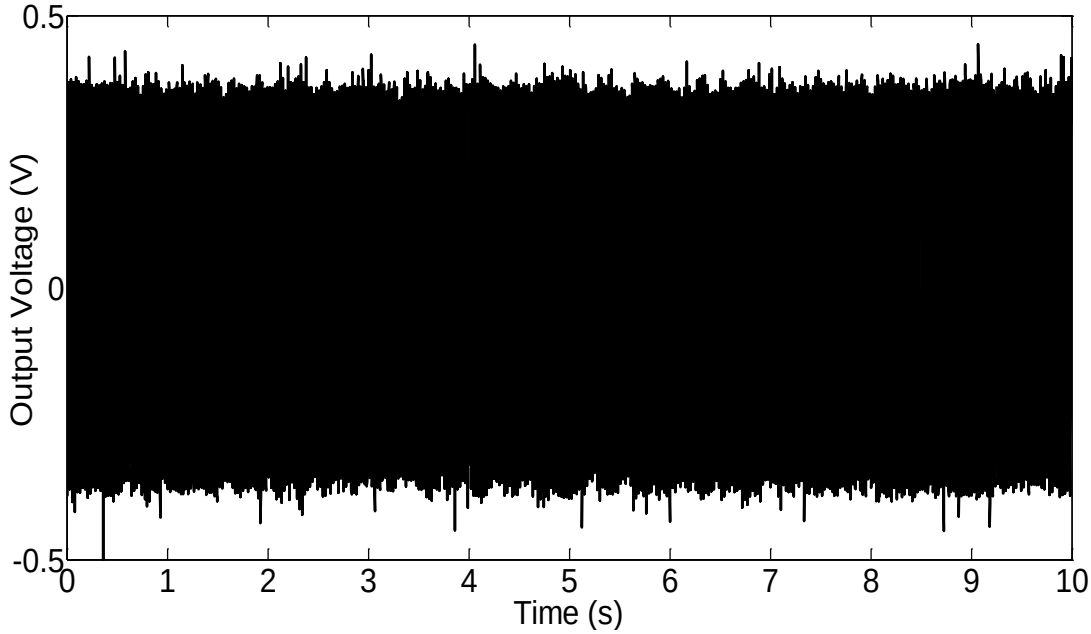

Figure 26: Time Domain Output Voltage over a Larger Sampling Period

Figure 27 shows the changes of the RMS value of the voltage signal in Figure 26 over time. The reading is made when the RMS value of the output voltage reaches a final value. The software also shows the FFT in real-time so that the operator knows whether or not other frequencies exist in the vibrations as noise and other temporary instabilities (Figure 28).

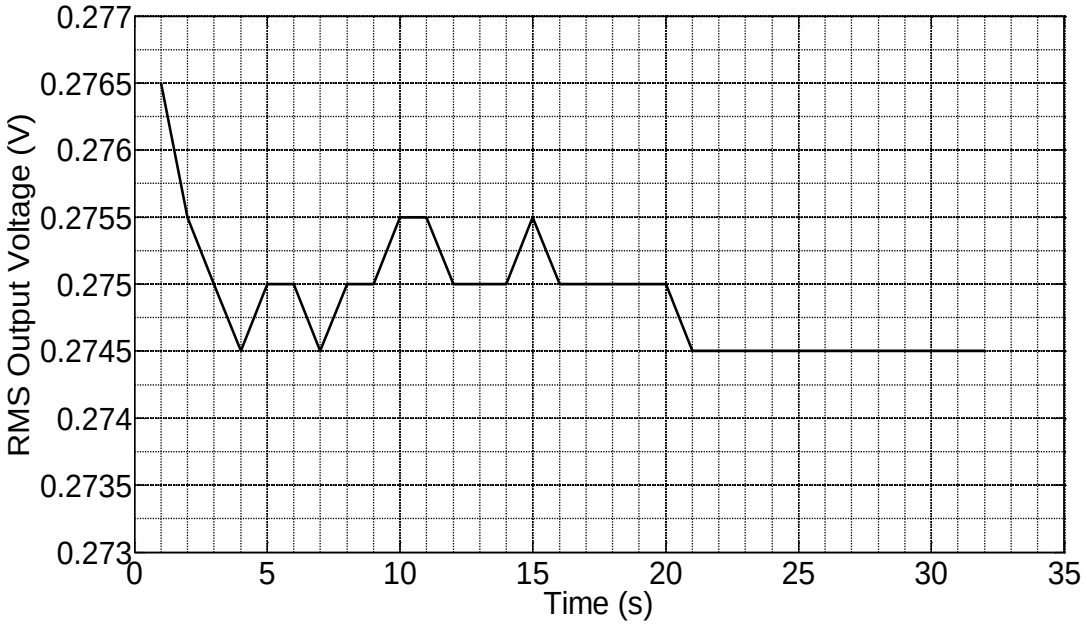

Figure 27: RMS of the Measured Voltage Signal

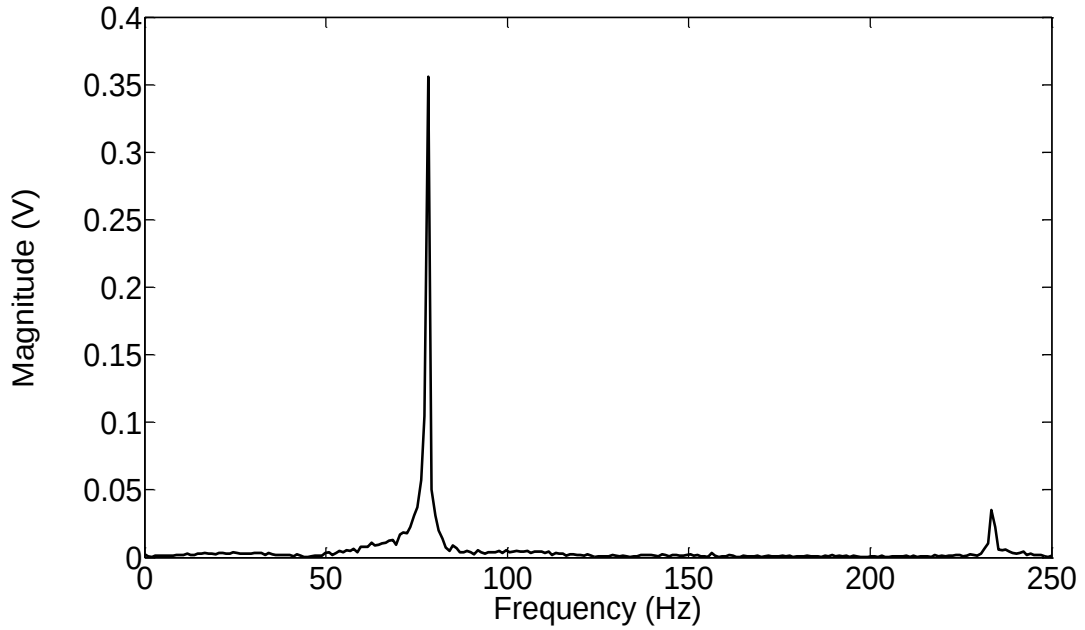

Figure 28: FFT of the Voltage Signal

Note that the magnitude of the voltage in the FFT graph belongs to the characteristic resistor of the DAQ circuit (Figure 24) for load resistance of $1195\ k\Omega$ and is not the total output of the PVDF. The actual output voltage of the system is calculable by:

$$V_a = \frac{R_l + R_c}{R_c}\, V_c$$

Where V_a and V_c are the actual and characteristic voltages, respectively. Therefore the total output voltage can be calculated as Figure 29.

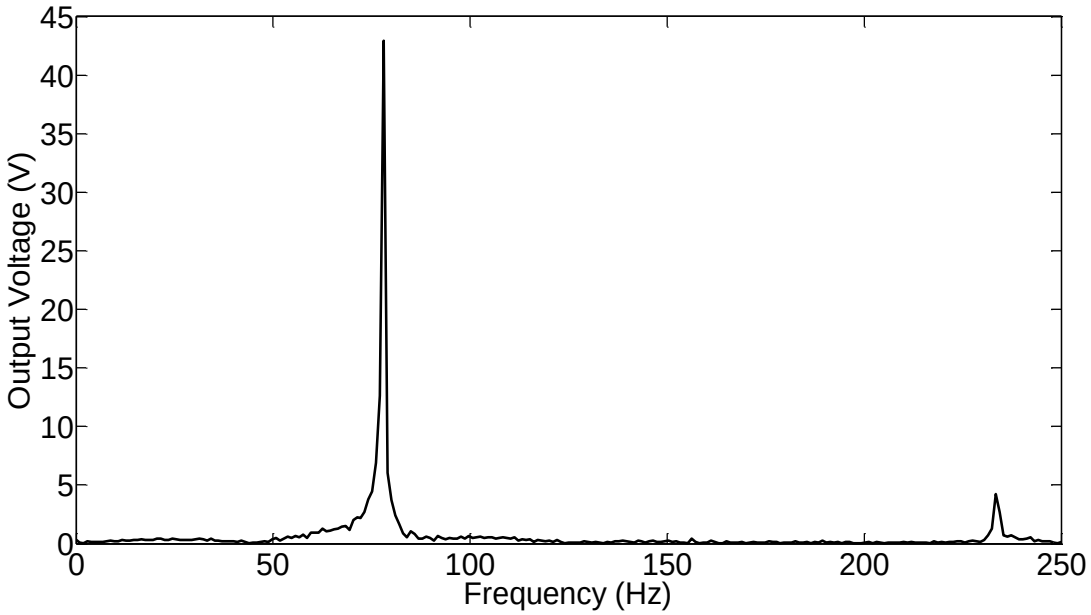

Figure 29: Total Output Voltage of the PVDF

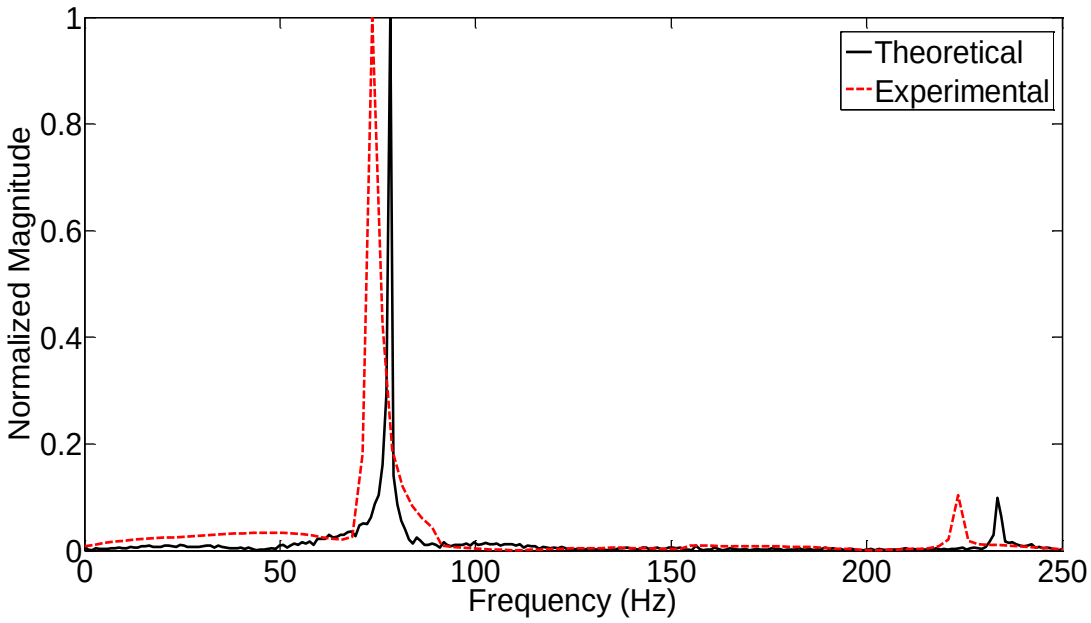

Figure 30: Frequency Verification of the Theoretical Output Voltage

It can be seen in Figure 29 that the two peaks observed in the theoretical investigation are present in the experimental results as well. In fact, as demonstrated in Figure 30 the theoretically calculated frequencies of the two peaks, are with less than 10% error average. Note that the y-axis shows the normalized magnitudes of frequency contents to show the error in calculation

of the peak frequencies. The magnitude of the theoretical output voltage results, however, is drastically different from the experimental results. Therefore further investigation is needed to find the source of this discrepancy. For the sake of completeness, we first present and discuss the other results of the wind tunnel experiments in regards to the output power of the fluttering PVDF and leave the assessment of the theoretical approach for the next chapter.

Experimental Results of the Generated Power

In order to calculate the generated power of the energy harvester, we use the RMS readings of the output voltage made available by the data acquisition program. The experiment is repeated for different load resistances to determine the optimal resistance of the PVDF film sensor. Also the patch is cut down to shorter lengths and output power curves are created.

Figure 31 shows the voltage curves at different load resistances and different lengths of the PVDF film.

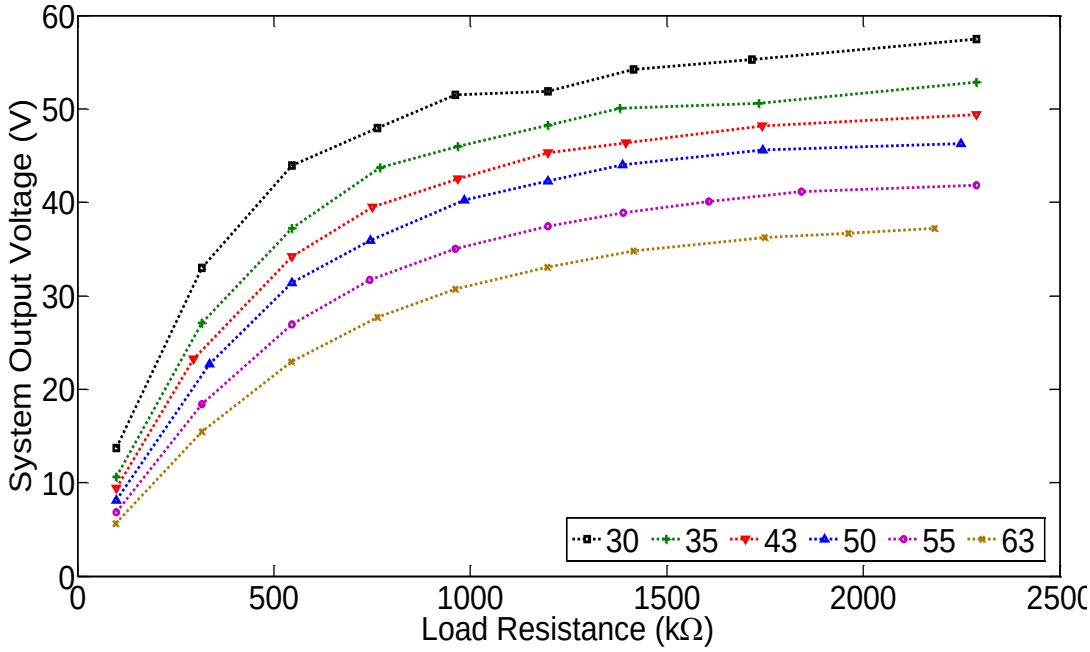

Figure 31: Output Voltage vs. Load Resistance for Different Lengths

As this figure shows, the changes of voltage are in agreement with the predicted trend from the theoretical analysis demonstrated in Figure 5.

Benefiting from the theoretical trend of Figure 5 between output voltage and load resistance, we use curve fitting on the data at 10 different loads to derive continuous variations of output voltage. According to Equation(15), the voltage-resistance curve has the form of:

$$V = \frac{a \cdot R}{1 + b \cdot R}$$

We use MATLAB™'s Curve Fitting Toolbox, to find a and b for each data set. The results are summarized in Figure 32.

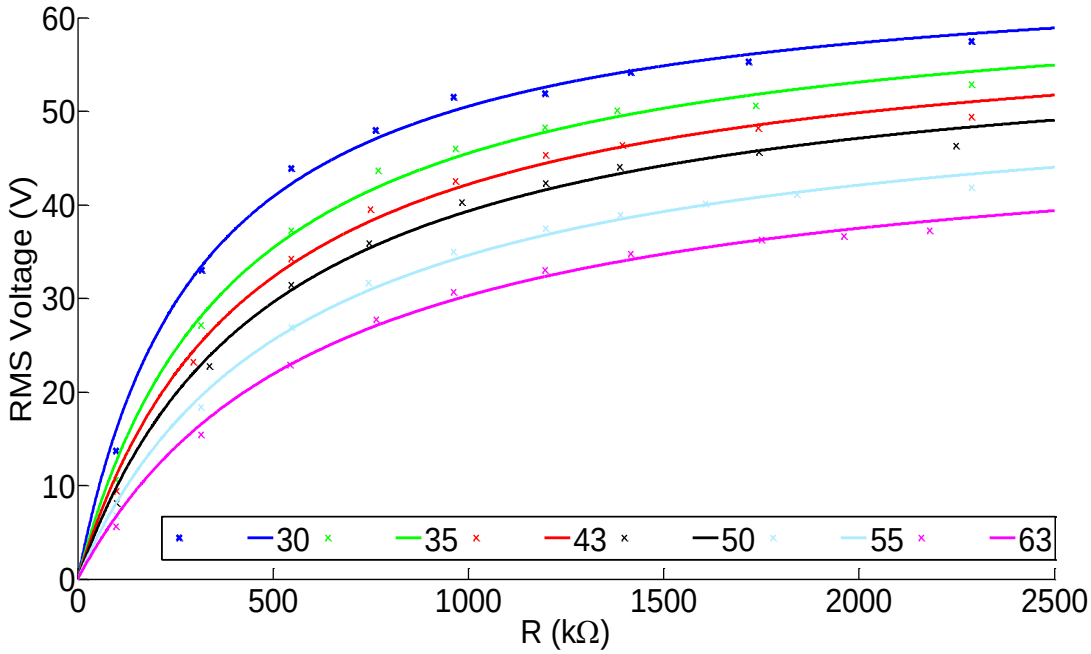

Figure 32: Voltage-Resistance Curve Fitting Results vs. Data

Based on these curves, the output power of the system can be derived using:

$$P = \frac{V^2}{R}$$

Figure 33 shows the output power of the energy harvester. As it can be seen in Figure 31 and Figure 33, the output voltage and the power generation increase with decreasing length of the PVDF. This is shown in Figure 34, where the maximum energy harvesting capacity is graphed with respect to the corresponding length.

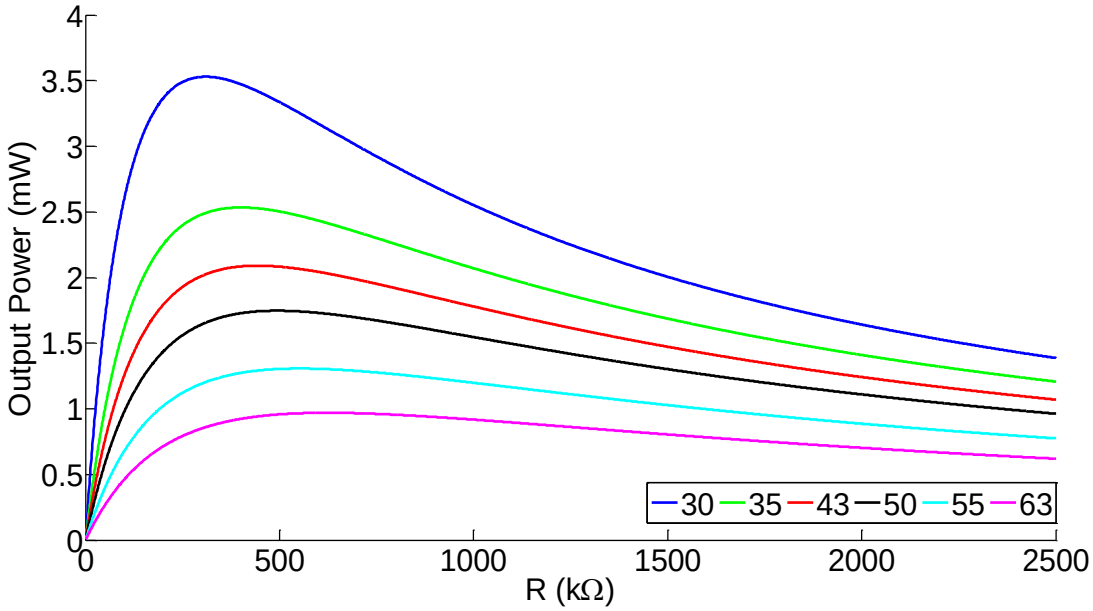

Figure 33: RMS of Generated Power vs. Load Resistance

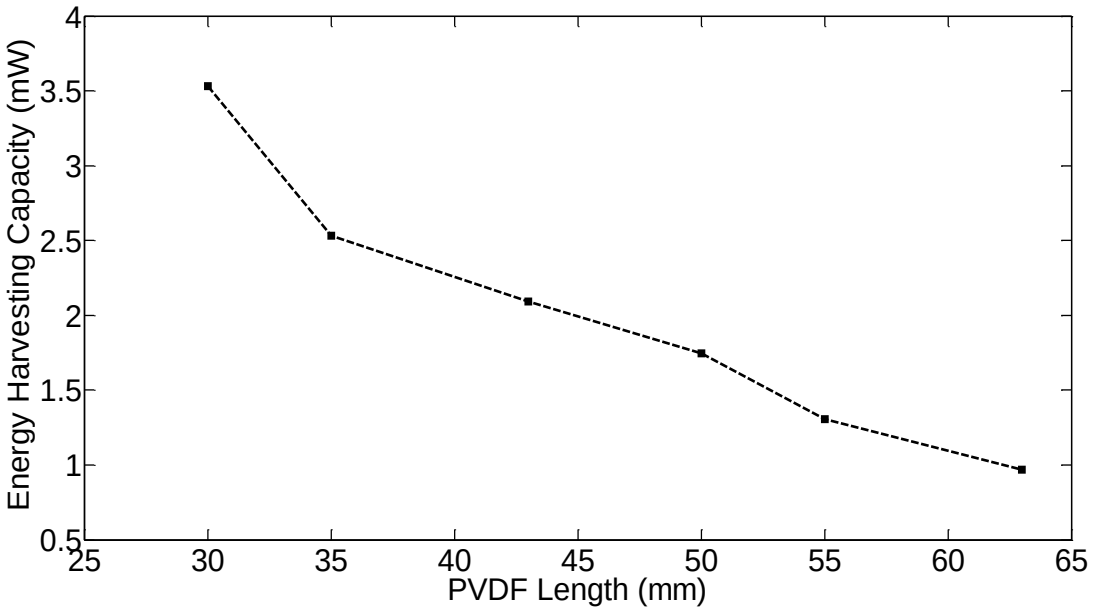

Figure 34: Energy Harvesting Capacity for Different Lengths

In order to explain the trend observed in Figure 34, we can use the FFT results of the data acquisition program and study the changes of flutter frequency with length of the beam. Figure 35 shows the main flutter frequency for both theoretical and experimental results. The main frequencies, as illustrated in Figure 35, increase with decreasing the beam length. This observation is consistent with the mathematical model of the piezoelectric energy harvester that higher vibration frequency leads to greater output

voltages. Also these results show that the theoretical approach has been able to calculate the flutter frequency for different lengths within an error margin of 10%.

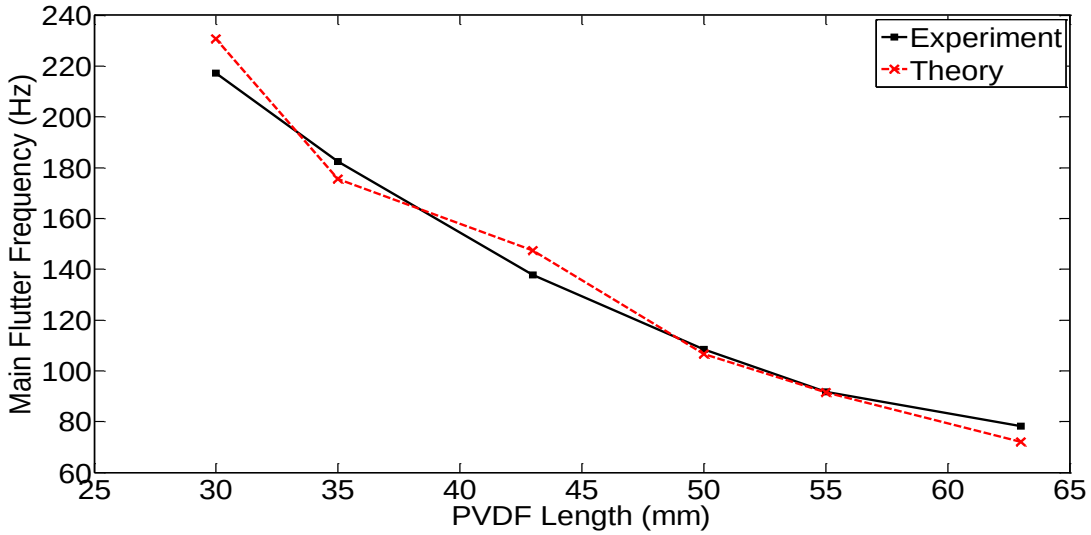

Figure 35: Main Flutter Frequency for Different PVDF film lengths

On the other hand, it is shown in Figure 36 that the optimal resistance increases rather linearly with the length of the PVDF, which along with the higher voltages produced by the shorter beams, leads to an increase in energy harvesting capacity with decreasing length.

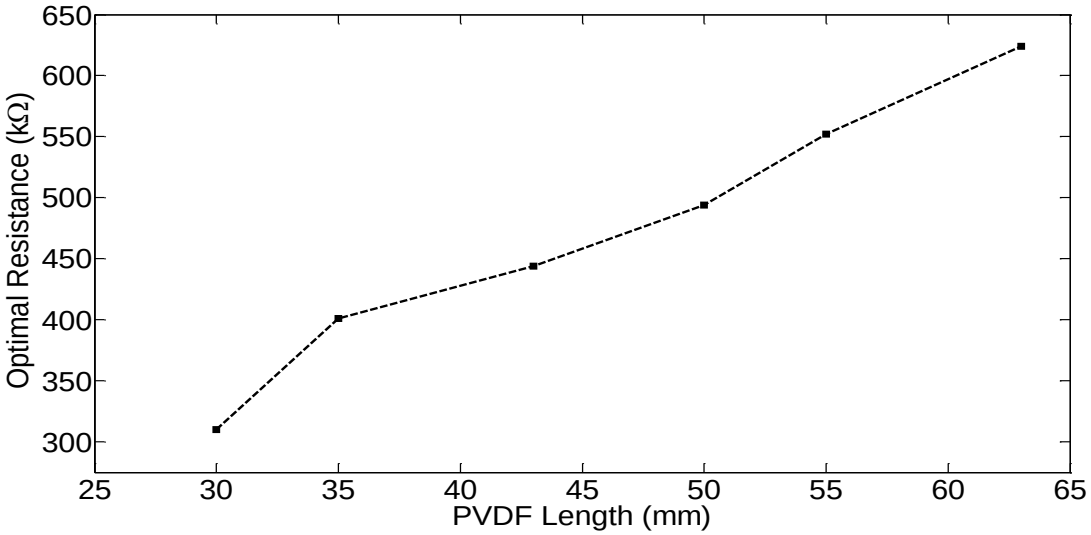

Figure 36: Optimal Resistance at Various PVDF Lengths

Although a higher power harvesting capacity is observed for shorter lengths of the PVDF, since the critical velocity is also higher, it means a higher power is

needed to drive the energy harvester. Therefore, the power needed to create such a flow should be compared to the output power of the harvester to investigate the power harvesting efficiency of the system as well. In order to find the driving power, the flow head loss in the duct is calculated using the Darcy-Weisbach equation [44], where h_f, f_d, L, D, V and g are the head loss, friction coefficient, length and diameter of the duct, fluid velocity and local gravitational acceleration, respectively:

$$h_f = f_d \frac{L}{D} \frac{V^2}{2g}$$

Once the head loss and hence the pressure difference is calculated, the driving power can be found by multiplying the pressure drop (Δp) and the flow rate (Q) as:

$$P = \Delta p \, . \, Q$$

Figure 37 shows the comparison between the driving power of the system and the generated power. As it can be seen in the comparison results, a rather similar ratio between the driving power of the flutter and the energy harvesting capacity is observed across all lengths of the PVDF. Note that, the driving power is here calculated as the total power needed to maintain flow in the duct of our experiment, where only a small portion of the flow energy is transferred to the PVDF for conversion. Since it is not possible to exactly find this portion, the general driving power is used as a measure for comparison.

The ratio of the power harvesting capacity to the driving power is demonstrated in Figure 38. According to the results, the efficiency of energy harvesting does not change significantly for the shorter lengths of the PVDF, while it is lower for longer lengths. These results also indicate a maximum point for the $43\,mm$ PVDF, but further research will be needed to find conclusive results on the possibility of optimum dimensions and configurations.

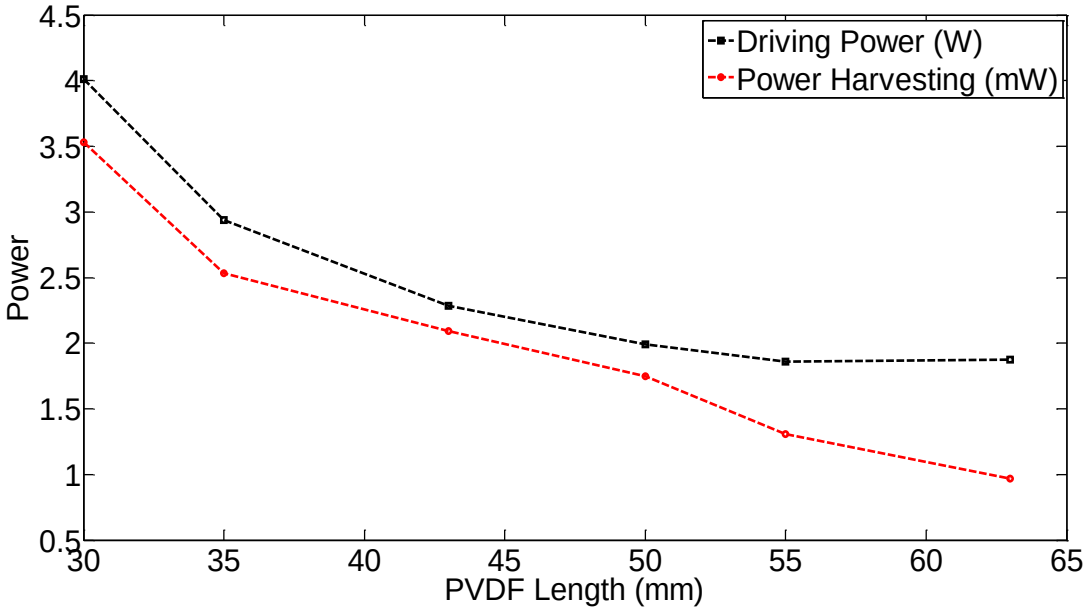

Figure 37: Comparison of Driving Power and Harvested Power

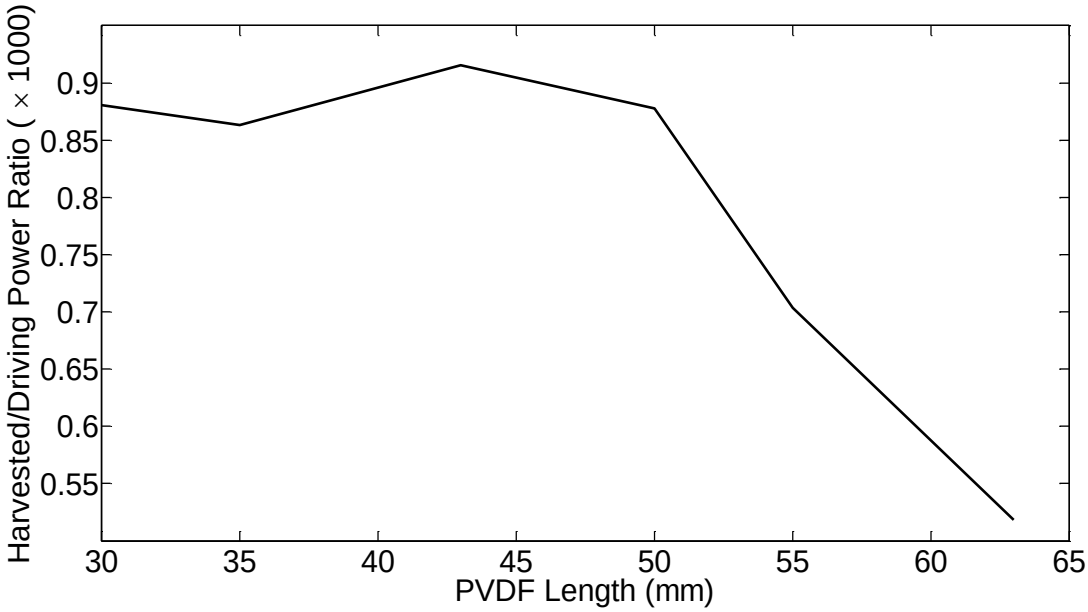

Figure 38: Energy Harvesting Ratio

The results of the experimental analysis show a radically higher power harvesting capacity of the proposed energy harvester than theoretically calculated. This finding shows that flutter-based energy harvesting is definitely a sufficient source for powering of remote sensor networks. The discrepancies between the magnitude of the theoretical and experimental output voltages, however, have to be investigated.

Observations on Actual Flutter Behaviour

Figure 39 shows an instance of the beam's vibration, photographed from the top. As it can be seen in the figure, tip displacement is comparable to the length of the beam. In the theoretical approach, however, the maximum tip displacement of the beam was calculated to be a few tenths of a millimetre (Figure 15). Therefore the vibrations exceed assumed limit where the tip deflection is supposed to be just an order to magnitude larger than the thickness of the beam. The common theoretical models of flutter in the literature follow the same assumption. Hence, a specific research project would be needed to improve the flutter theory in our system. As the focus of our study is to investigate the energy harvesting potential of a fluttering PVDF, a complete flutter analysis is beyond the scope of this thesis.

Figure 39: Instance of the Fluttering of the PVDF

Since the frequency content of the theoretically calculated output voltage matches the experimental results in terms of the frequencies of the peaks, it would be safe to assume that the frequency content of tip deflection found by the theoretical approach has also been correct as well. Here we seek to use the experimental observations to correct the magnitude value and reassess the results. It was shown in Figure 19 that 92% of the theoretical tip deflection is dominated by the first peak, leading to a vibration that seems to be containing a single frequency. This observation was repeated in the theoretical voltage of Figure 21 and also the experimental voltage readings of Figure 25 and Figure 28. Therefore by using Figure 39 we can roughly

measure the maximum tip deflection of the PVDF and use it to correct the theoretical tip deflection frequency content by a factor. This rough estimate is found by taking the known width of the experiment duct (Figure 23) as a reference length to calculate the scale of the photo. Then the tip deflection is measured by an ordinary ruler and the scale is applied to find an estimate of the actual value, which is $3.5\ cm$. By allocating this value to the two peaks based on their different contributions, we can find Figure 40 for the corrected value of tip deflection.

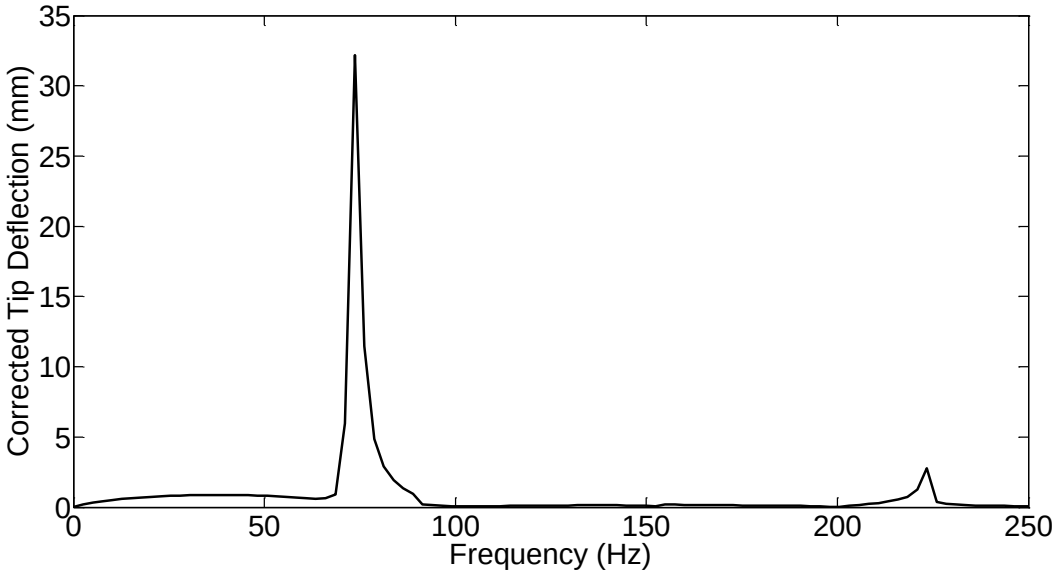

Figure 40: Corrected Theoretical Tip Deflection

Now by applying the theoretical transfer function of Figure 22 we can recalculate the output voltage of the PVDF. The resulting output voltage is shown in Figure 41 in comparison to the experimental results. This figure shows tremendous improvement in terms of estimating the actual output voltage of the energy harvesting system. The value of the second peak matches the experimental results while the first peak is calculated 16% higher than the actual value. This discrepancy is addressed further by designing an experiment to measure the elctromechanical transfer function of the PVDF and compare the results to the transfer function found through the theoretical approach (Figure 22).

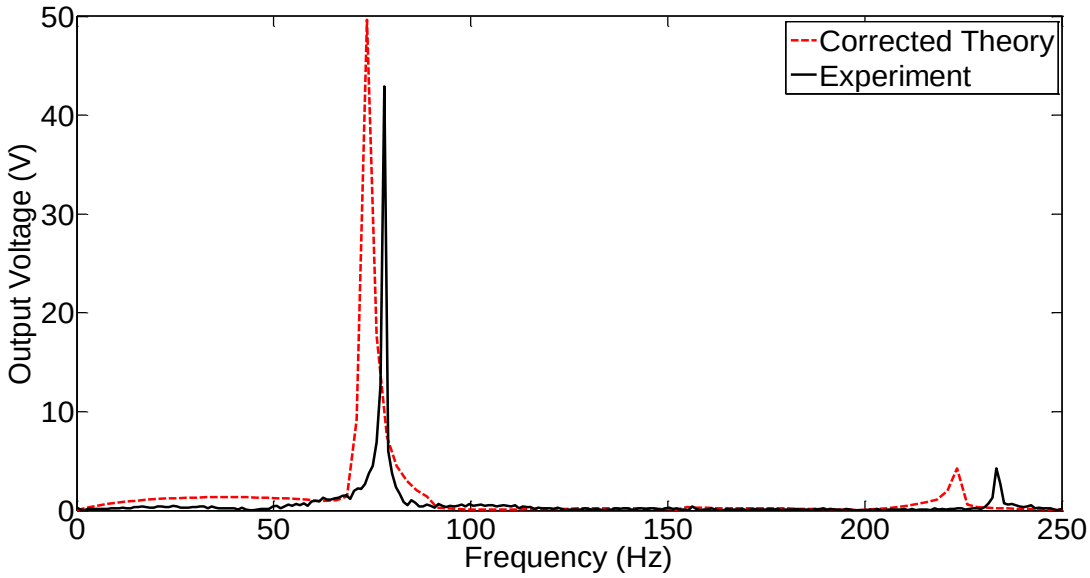

Figure 41: Corrected Theoretical Voltage vs. Experimental Results

Electromechanical Conversion of PVDF Patch

Due to the lack of scientific data on commercially used piezoelectric film sensors, providing an exact mathematical model for electromechanical behaviour is not always possible. The specification sheet of the commercial film sensors is not very detailed about the inner structure of these items. However, this knowledge is essential to design of energy harvesters. Hence, the fact that we assumed the PVDF patch as a unimorph piezoelectric power harvester can be the source of the difference between the anticipated and actual output voltage values of the first peak. In order to examine this issue, a shaker experiment was designed to find the transfer function of the PVDF for electromechanical conversion. This innovative idea aims at finding a substitute for situations where an exact modelling of the energy harvester patch is not possible.

According to the theoretical modeling of the piezoelectricity of the beam, the output voltage is a function of both deflection and frequency. On the other hand, knowing the oscillation details of a single point on the structure is enough for determining the motion of the entire body, based on the mechanical properties of the beam. Therefore, we can use the output voltage of the film sensor for different frequencies and tip displacements to

derive a transfer function. Once this transfer function is found, we can calculate the electrical output of a vibrating piezoelectric patch, by knowing its mechanical motion. With reference to the tip velocities of the system identification test, we calculate the electromechanical transfer function of the PVDF film by dividing the voltage frequency responses by the measured tip deflection.

In this set of shaker tests, the excitation frequency of the shaker (Figure 7) is raised to include three natural frequencies of the beam. The tip deflection and the output voltage of the beam are measured and the conversion factor is taken as the voltage divided by the tip deflection.

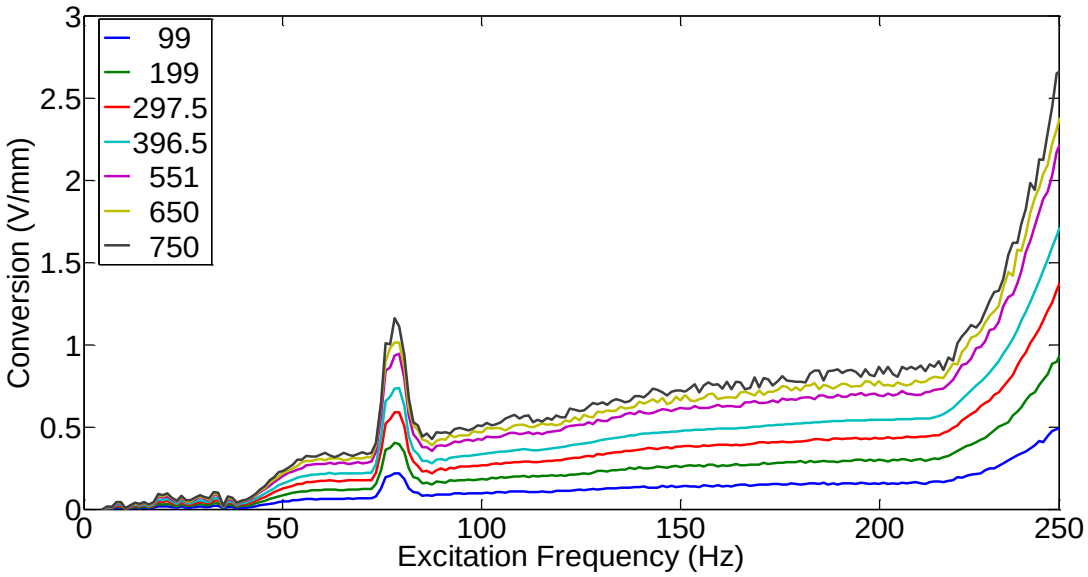

Figure 42: Transfer functions at Different Load Resistance Values

Figure 42 shows the transfer functions at different values of load resistance. Note that these low voltage values are the response of the system to shaker displacements of $0.5\ mm$. It was mentioned earlier that the output voltage of the system varies for different loads. That is why the transfer function, is different for various load resistances. Therefore results are corrected considering this effect and shown in Figure 43, where the resulting curves overlay with negligible error. This error is due to measurement resolution. These curves show that the conversion factor changes for different vibration frequencies. This is contrary to the theoretical finding of Figure 22 with a constant transfer function. Therefore the assumptions made in modelling the

PVDF film have not been entirely correct and only a part of the actual voltage is truly calculated.

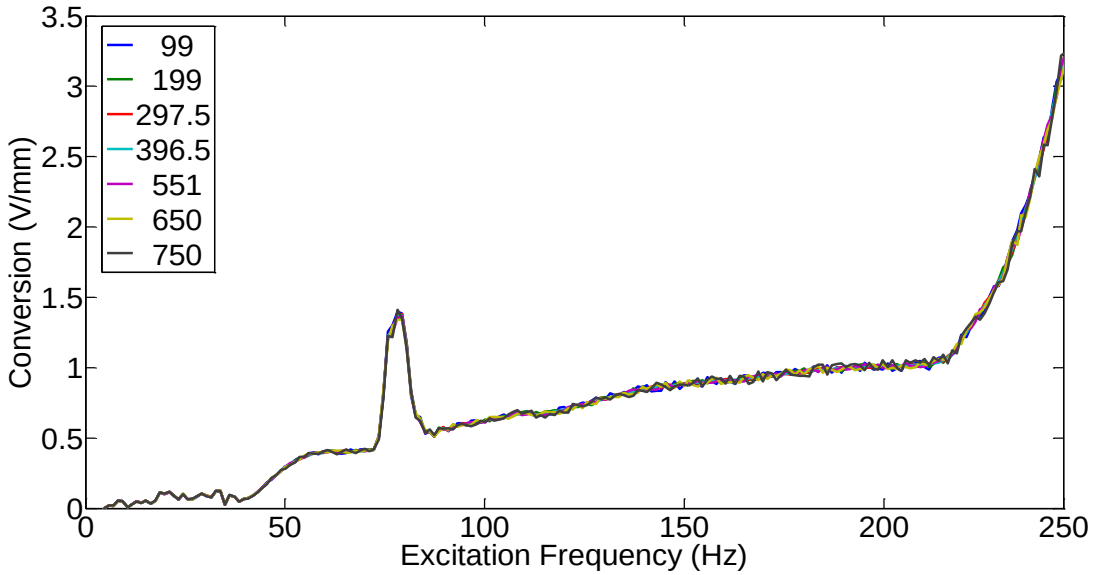

Figure 43: Transfer Functions Corrected for Test Load Resistance

Combining these transfer functions with the corrected tip deflection, we can determine the output voltage of the beam in frequency domain (Figure 44).

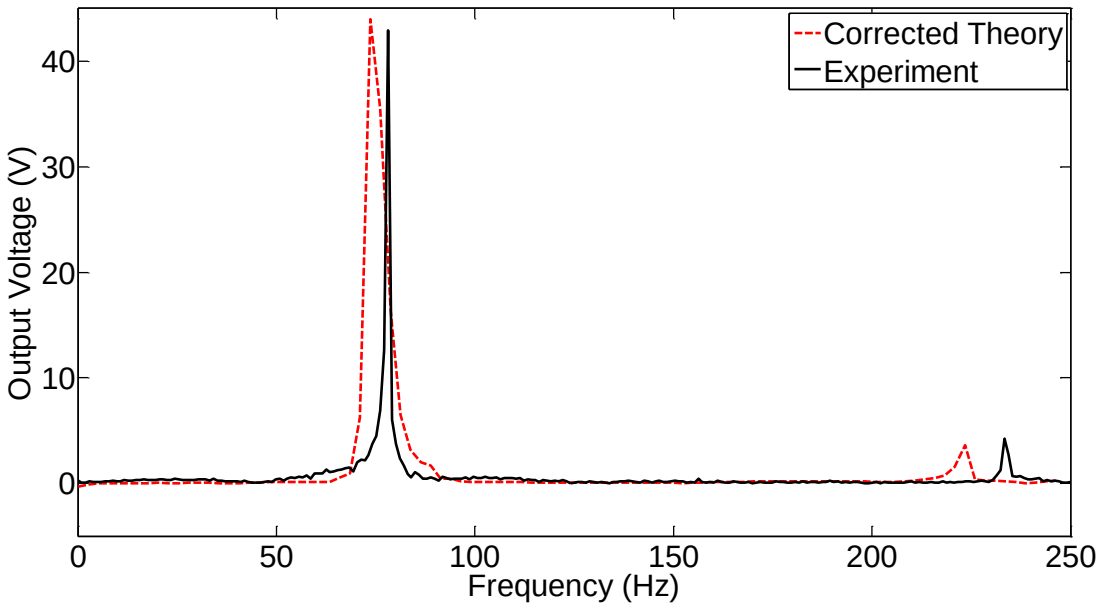

Figure 44: Double Corrected Output Voltage vs. Experimental Result

As illustrated in this figure, the magnitude of the first peak is calculated with a 3% error margin. The method proposed here to find the transfer function of the PVDF shows great potential in substituting mathematical modelling in

situations where the inner structure of a piezoelectric energy harvester is unknown.

Chapter 4:

High-Speed Video Large Deflection Vibrometry

Based on the method used in the previous chapter to correct the theoretical tip deflection values, we here propose an innovative method for measurement of vibrations that involve large deflections. As shown in Figure 39, the tip deflection of the fluttering PVDF is several times larger than the deflections associated with the shaker test used for system identification. As laser vibrometry is not able to measure displacements over a few millimetres, using images is one of the few options to capture the dynamics of motion.

Thanks to the recently marketed personal digital cameras, high speed photography is made available at a feasible expense. This will provide a novel solution to measuring high deflection vibrations. Image processing technology has created numerous techniques to analyze the video image of a moving object. The picture of the structure can be dealt with manually or automatically to regenerate the motions in the software. In this project, we use a Nikon 1 J1 digital camera that can shoot video up to 1200 frames per second. To increase the picture quality, light projectors are used to enhance the visibility of the object. Meanwhile, since the PVDF film sensor is of bright color, a black background is attached to the Plexiglas duct to increase the contrast of the image (Figure 39). In this measurement technique, we cover the beam in each frame by points to approximate the shape of the deformed beam. These points construct an array that corresponds to the instance each picture is taken. By combining all the instances of the beam, the flutter motion is reconstructed in the software and the frequency domain data is generated using a Discrete Fourier Transform (DFT).

The proposed large deflection vibration measurement process is done by a program designed in MATLAB™. In this program we start with the video

image of the flutter, captured by the Nikon camera. This footage is then analyzed frame by frame and the approximation points are located on the beam by mouse click (Figure 45).

Figure 45: Locating the Approximation Points on the Beam

An important factor that has to be considered in this phase of the analysis is the number of the frames we include in the point placement. This number determines the accuracy and the reliability of the DFT algorithm. Nyquist-Shannon Sampling Theorem requires the number of sample points to be two and a half times the maximum desired frequency of measurements [44]. On the other hand, for any approximation data derived through a numerical technique, there needs to be a validation phase to show that increasing the input data population will no longer affect the results. These two controls are considered in this approximation method. Once a desired number of frames are acquired, the approximate shape vectors undergo *normalization* and *parameterization* to be ready for DFT analysis.

Normalization: Since placing points on a picture using the computer mouse is not a precise procedure, corrective action needs to be taken so that the clamped condition of the beam is satisfied. Therefore, the locations of all the points in a single frame of the movie are changed to positions relative to the first point placed on the frame. This will adjust the first point to be $(0,0)$ and ensures that all the approximated beam vectors coincide at the clamp. Another shortcoming of manual point placement is that the length of the approximated beam varies for different frames of the movie. Although the

length of the beam changes due to the large deformation of the structure, these elongations are negligible compared to the tip displacement of the beam. To correct the length variation error, the relative positions of the points on the beam are divided by the calculated length of the vector. As a result, all the approximated beams will have a unit length. The mean length of all the approximated beams will later be used to scale the results to actual measures.

Parameterization: There are some instances of the beam vibration where a part of the structure is lying on a vertical line. This means that the points move both vertically and horizontally, thus eliminating the option of monitoring the vertical changes in position to measure the displacements. An alternative approach is to use a polar coordination system where the location of each point is determined by its distance and angle relative to its previous point. In order to find the frequency domain representation of the flutter vibration, the measurements have to undergo a Fourier transform, which requires measurement samples corresponding to a constant parameter. Meanwhile, different shapes of the beam require a particular point density at various locations so that no feature of the deformed shape is left out. This means that the number of the points as well as the local position of i-th point (location on the length of the beam) will vary for each of the frames. Therefore we need to employ an interpolation technique to convert the preliminary data to a set of approximated beams where the motion of a specific point on the beam can be followed for all the frames. This is done by dividing each of the shapes into 50 subsections of equal length and mapping the approximated shape onto these locations.

Figure 46 shows the result of parameterization of the normalized approximated beam. The approximated beam is divided into 50 segments of equal length and the angles of the original segments are used to determine the angles of the generated segments. Since the lengths of the original segments are not necessarily an integer product of the length of the new segments, a degree of error exists. However, the maximum length

computation error of this method was found to be below 2 percent, which is acceptable given the approximate nature of the measurement technique

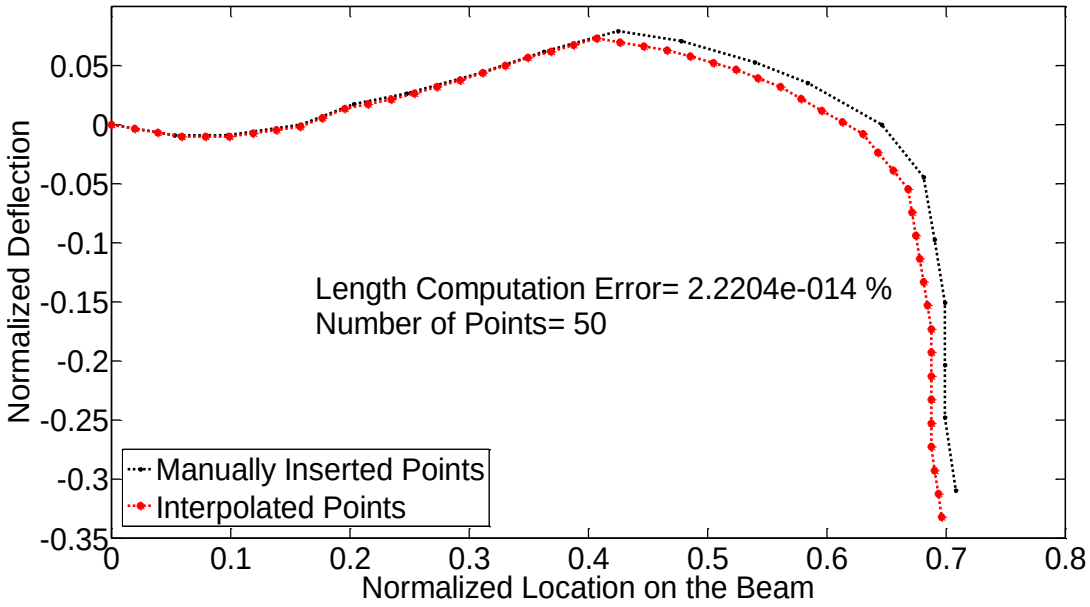

Figure 46: Parameterization Of the Approximated Beam

The parameterization phase results in an array of angle values for each segment measured for different instances. In order to calculate the frequency content of the fluttering PVDF, the variations of the angle of each segment are used as time domain samples. These time samples can be used to generate a frequency domain representation of the vibrations by means of a Fourier Transform. Due to the skipped blurry frames, the Fast Fourier Transform (FFT) available in MATLAB™ cannot be used for frequency analysis. Hence, a DFT function is coded based on the general form of DFT:

$$F(\omega) = \frac{2}{N} \cdot \sum_{i=1}^{N} x(t_i) \cdot e^{-j\omega t_i} \qquad (18)$$

In Equation(18), t_i is the time corresponding to the $i-th$ sample. This formula calculates the amplitude of the frequency response (F) at each frequency (ω) where N is the total number of data samples.

Examining the Deflection Measurement Method

Before employing the algorithm to measure the actual footage of the fluttering PVDF, a test run was conducted to see if this method will be able to achieve a correct frequency domain representation. To that end, a hypothetical beam was considered to be vibrating with the first two modes, each at a given frequency. Then the point placement phase was simulated by considering random errors in locating the points, the number of the points on each frame, and whether or not a frame will be included. Figure 47, shows the DFT of the tip displacement resulting from this approximation overlaid with the FFT of the same variable calculated through the original data for the vibration of the hypothetical beam.

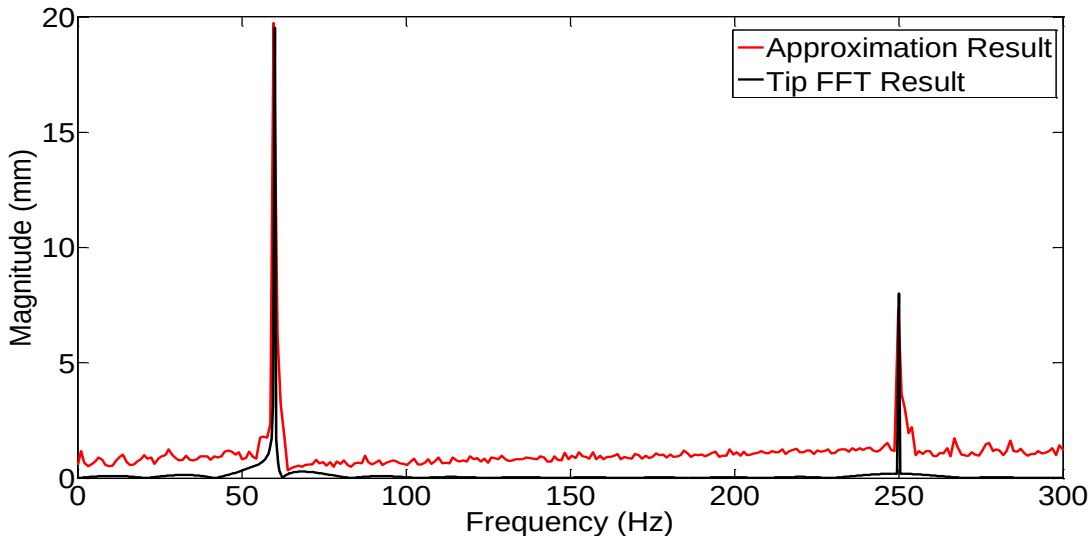

Figure 47: Approximated Tip Displacement DFT vs. Actual Tip Displacement FFT

The results show agreement with their expected value in finding the frequency and the magnitude of the peaks. Nonetheless, due to the high randomness considered for this simulation, error is observed in other frequency ranges. This error cannot be deemed negligible because its order of magnitude is comparable to the second peak. However, as the magnitudes of the peaks are hypothetically determined in this test, it is safe to say that this constant error will be negligible to the high amplitudes associated with the flutter vibration.

It is to be noted that despite the minimum sample requirements forces by Nyquist-Shannon Sampling Theorem, the algorithm can approximately capture the frequency of the peaks at lower number of frames. By raising number of samples, the approximation becomes more accurate and eventually reaches a plateau, where reliable measurement can be reported.

Preliminary Investigation

In this section the results of applying the video vibrometry on the video footage of the fluttering PVDF are presented. The movie is shot at 1200 frames per second, so even a 3 second movie can provide the algorithm with enough samples to satisfy Nyquist-Shannon Sampling Theorem. As mentioned earlier, another criterion to determine whether the number of the frames have been adequate is to monitor the variations in the results due to increasing number of frames. Once the goal parameter of the measurement does not exhibit significant change for higher number of frames, the process can be terminated. The goal parameters of our measurement are the location of the peaks in the frequency domain data of the tip deflection.

In order to gain a perspective on the frequency content of the fluttering PVDF, a preliminary analysis is performed by calculating the DFT for all the 50 points of the beam and averaging the results. This is because even though in Galerkin's decomposition we assume the response to be a sum of the natural modes of the beam, flutter is not realistically a modal vibration. As it is apparent in a waving flag, some parts of the structure might be temporarily stagnant while the rest of the structure is undergoing drastic deflections; a fact observed in our experiments as well. Therefore, by averaging the DFT results for all the points on the beam, we can obtain a general understanding on the frequency content. As it can be seen in Figure 48, three prominent peaks are visible in the graph with frequencies of $75.3\ Hz$, $150.6\ Hz$ and $225.8\ Hz$. The second frequency is precisely twice the first one, indicating an *aliasing frequency*. Aliasing frequencies are a side product of the DFT procedure, where increasing the sample count to capture a higher frequency peak leads

to the appearance of multiples of the lower-frequency peaks in the frequency domain.

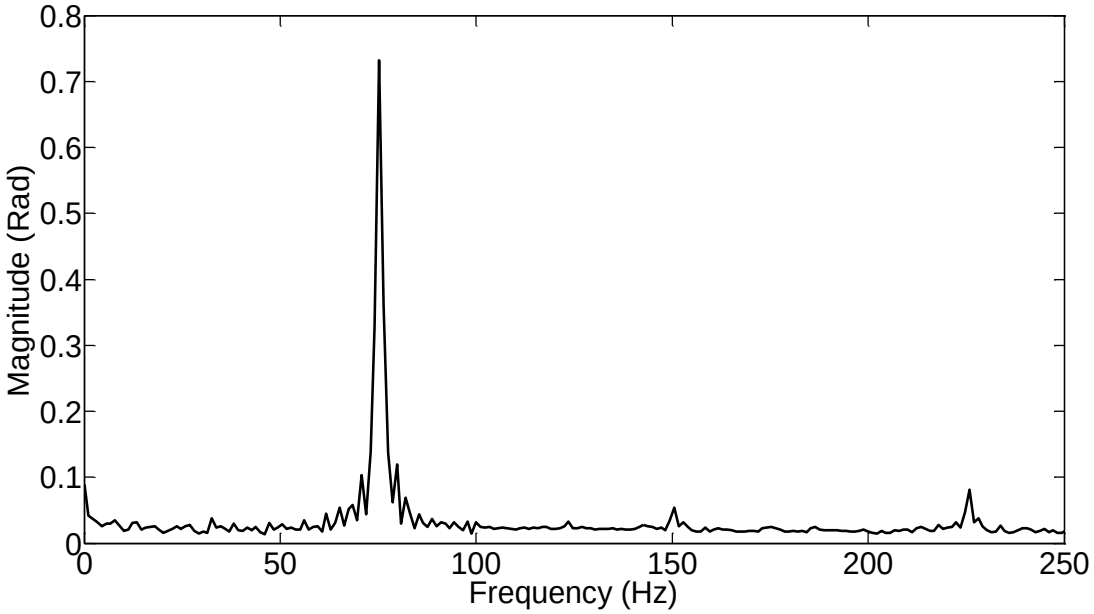

Figure 48: Average DFT for the Variations of All Segments

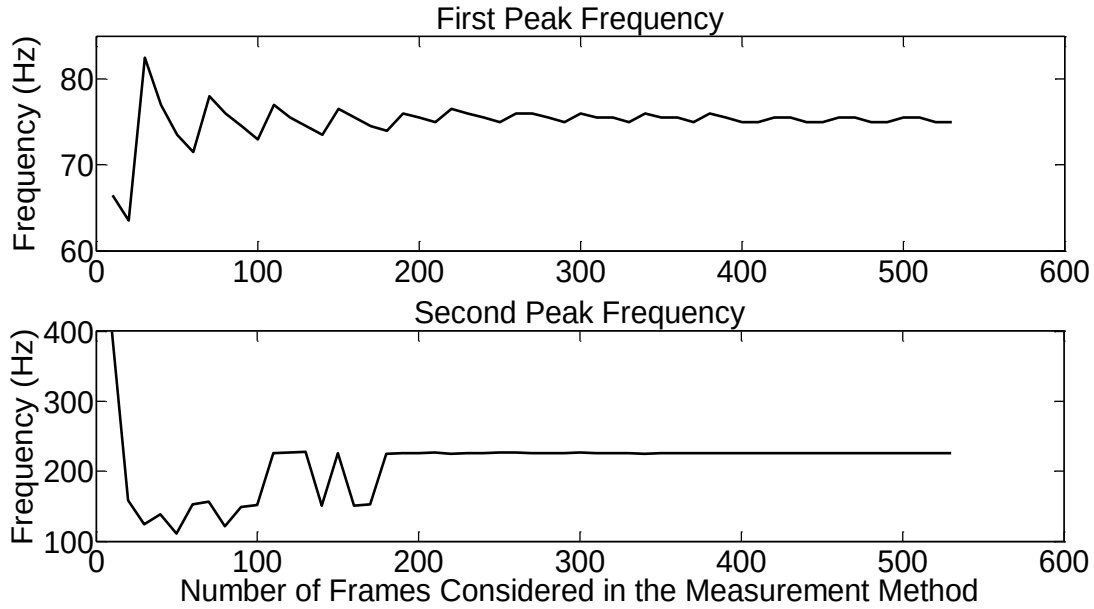

Figure 49: Convergence of the Calculated Frequencies of the Peaks

In Figure 49, the number of frames is increased from 20 to 530 and DFT is performed on the data to calculate the frequency content of the vibration. For lower frame counts, the peak locations change very drastically but the changes attenuate beyond a certain point and the frequencies of these peaks

converge to a final value. It can thus be concluded that the minimum number of frames for a reliable frequency response is 500.

Measurement Results for Tip Deflection and Output Voltage

Based on the results of the previous section, we can now proceed to calculating the frequency content of the fluttering PVDF's tip using the video vibrometry (Figure 50). Two peaks with the same frequencies as the experimental voltage values in Figure 30 are observed in the experimental results. Based on the combined magnitude of the peaks of Figure 50 we find the total tip deflection to be $3.45\ cm$. This shows that the value of $3.5\ cm$ measured using a ruler is correct within 1.5% error margin.

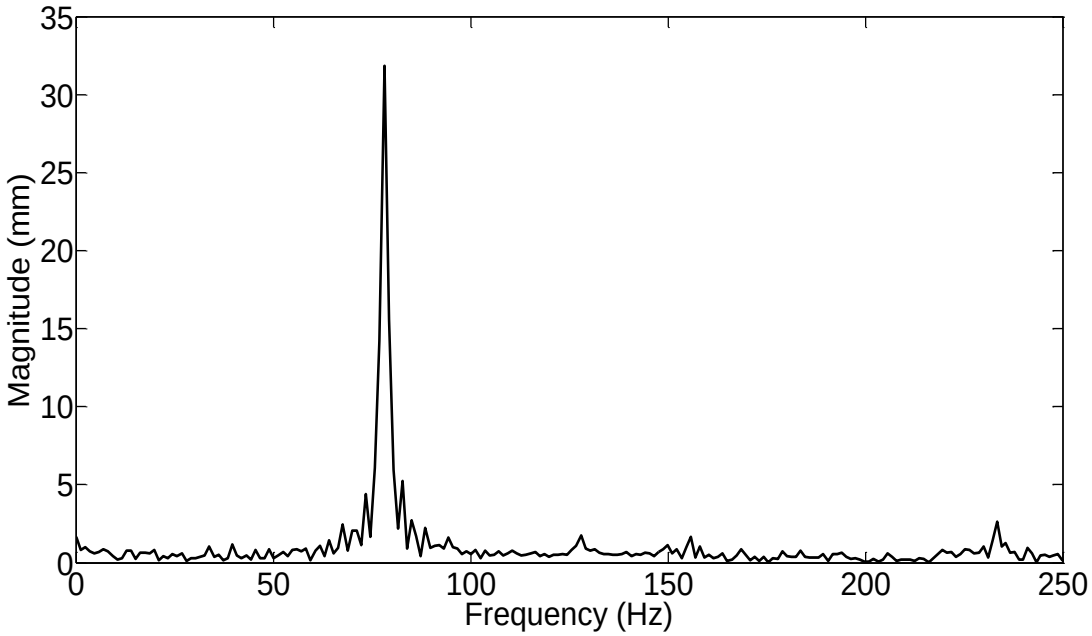

Figure 50: Calculated Frequency Content of Tip Deflection

We can also use the transfer functions of the PVDF (Figure 43) to compare the results of the video vibrometry with the experimental output voltage data. As demonstrated in Figure 51, video vibrometry has been able to calculate both frequency and the magnitude of the peaks of the voltage frequency content.

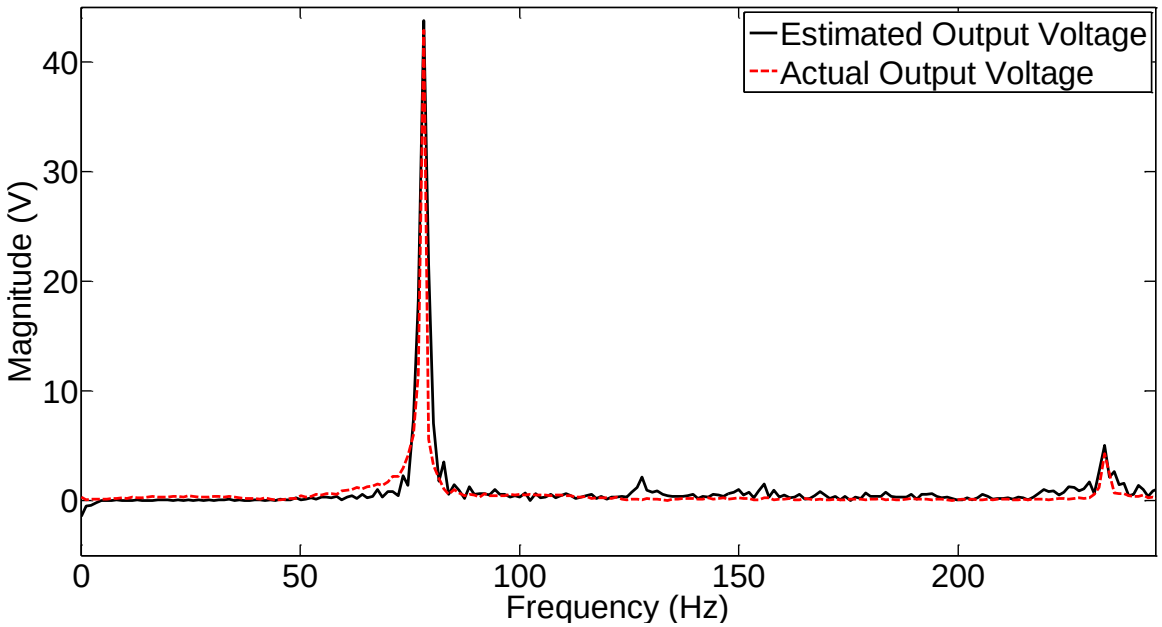

Figure 51: Video. Experimental Data

Chapter 5:

Conclusion and Future Directions

Conclusion

In this project an energy harvester concept was proposed for generating electricity from the powerful vibrations associated with flutter of flexible structures. Benefiting from the flexibility of the piezoelectric PVDF film sensors, we designed an energy harvesting device to be able to provide power to remote sensor networks. The dynamics of this device was investigated through theoretical modeling and the output power was calculated. The theoretical approach proved to be capable of finding the onset of flutter and the frequency content of the output voltage. In order to find the magnitude of the vibration, empirical measurement techniques were designed to complement the shortcomings of the conventional models. These techniques were used to estimate the output capacity of the harvester. The results were validated by the experiments, to prove the utility of the proposed techniques. Finally, the energy harvester was shown to be capable of producing up to $3.5mW$, which compared to the needs of industrial sensors and transmitters, will be adequate for powering the network [43].

Further, inspired by the simplicity and accuracy of the empirical model in measuring the tip deflection amplitude, a video vibrometry technique was designed. Benefiting from image processing, the proposed system was found to be accurate in measuring vibrations with large deflections.

Future Directions

- A more sophisticated mathematical model, capable of demonstrating the large deformation of the fluttering PVDF can be used to repeat the same investigation and examine the trade off between the added computation and the higher precision attained.

- The ratio between the power harvesting capacity and the power needed to drive such a harvester can be further investigated to find possible optimum dimensions and parameters for the design.

- The image processing method for measurement of high deflection vibrations can be automated to avoid the time-consuming phase of approximating the deformed beam by manually added points. This will also increase the accuracy of the technique and may lead to further capabilities of this solution.

- The findings of this project regarding the dependencies of the power generation capacity on the parameters of the system can be used to perfect the design and develop a commercially feasible device.

Works Cited

[1] S. Priya and D. J. Inman, *Energy Harvesting Technologies*, First Edition ed. New York: Springer, 2009.

[2] D. A. Adamko and J. D. DeLaurier, "An Experimental Study of an Oscillating-Wing Windmill," in *The Second Canadian Workshop on Wind Engineering*, Varennes, Québec, Canada, 1978, pp. 64-66.

[3] W. McKinney and J. D. DeLaurier, "The Wingmill: an Oscillating-Wing Windmill," *Journal of Energy*, pp. 109-115, 1981.

[4] K. H. Ly and V.A. L. Chasteau, "Experiments on an Oscillating-Wing Aerofoil and Application to Wing-Energy Converters," *Journal of Energy*, pp. 116-121, 1981.

[5] J. F. Manwell, J. G. McGowan, and A. L. Rogers, *Wind Energy Explained: Theory, Design and Application*. New York: Wiley, 2002.

[6] T. B. Johansson, H. Kelly, A. K. N. Reddy, and R. H. Williams, *Renewable Energy: Sources for Fuels and Electricity*. Washington, D.C.: Island Press, 1933.

[7] M. A. Weimar, T. S. Paing, and R. A. Zane, "Remote area wind energy harvesting for low-power autonomous sensors," in *Power Electronics Specialists Conference*, 2006, pp. 1-5.

[8] A. S. Holmes, G. Hong, K. R. Pullen, and K. R. Buffard, "Axial-flow microturbine with electromagnetic generator: design, CFD simulation, and prototype demonstration," in *17th IEEE International Micro Electro Mechanical Systems Conferece (MEMS 04)*, 2004, pp. 568-571.

[9] J. J. Allen and A. J. Smits, "Energy Harvesting Eel," *Journal of Fluids and*

Structures, pp. 629-640, 2001.

[10] G. W. Taylor, J. R. Burns, S. A. Kammann, W. B. Powers, and T. R. Welsh, "The Energy Harvesting Eel: a Small Subsurface Ocean/River Power Generator," *IEEE Journal of Oceanic Engineering*, pp. 539-547, 2001.

[11] C. B. Caroll, "Energy Harvesting Eel," 6424079, 2003.

[12] LLC Humdinger Wing Energy. (2008) Technical Brief on Windbelt. [Online]. www.humdinger.com

[13] Ltd. Vortex Oscillation Technology. (2008) Hydrogenerators With Oscillating Wings. [Online]. www.vortexosc.com

[14] L. Tang, M. P. Païdoussis, and J. Jiang, "Cantilever Flexible Plates in Axial Flow: Energy Transfer and the Concept of Flutter-Mill," *Journal of Sound and Vibration*, pp. 263-276, 2009.

[15] T. Burton, D. Sharpe, N. Jenkins, and E. Bossanyi, *Wind Energy: Handbook*. New York: Wiley, 2001.

[16] M. Bryant and E. Garcia, "Development of an Aeroelastic Vibration Power Harvester," in *Proceedings of SPIE*, vol. 7288, 2009, p. 728812.

[17] A. Erturk, W. G. R. Vieira, Jr., C. De Marqui, and D. J. Inman, "On the energy harvesting potential of piezoelectric systems," *Applied Physics Letters*, vol. 96, p. 184103, 2010.

[18] Soon-Duck Kwon, "A T-shaped piezoelectric cantilever for fluid energy harvesting," *Applied Physics Letters*, vol. 97, p. 164102, 2010.

[19] S. Taneda, "Waving Motion of Flags," *Journal of Physical Society of Japan*, vol. 24, pp. 392-401, 1968.

[20] S. K. Datta and W. G. Gottenberg, "Instability of an Elastic Strip Hanging in the Airstream," *Journal of Applied Mechanics*, vol. 42, pp. 195-

198, 1975.

[21] J. Katz and A. Plotkin, *Low-Speed Aerodynamics*. New York: Cambridge University Press, 2001.

[22] C. Lemaitre, P. Hemon, and E. de Langre, "Instability of a long ribbon hanging in axial flow," *Journal of Fluids and Structures*, vol. 20, pp. 913-925, 2005.

[23] A. Kornecki, E. H. Dowell, and J. O'Brien, "On the Aeroelastic Instability of Two-Dimensional Panels in Uniform Incompressible Flow," *Journal of Sound and Vibration*, vol. 47, pp. 163-178, 1976.

[24] R. L. Bisplinghoff, H. Ashley, and R. L. Halfman, *Aeroelasticity*, First Edition ed. Reading, MA, USA: Addison-Wesley, 1955.

[25] M. Argentina and L. Mahadevan, "Fluid-Flow-Induced Flutter of a Flag," in *National Academy of Science of the United States of America*, vol. 102, 2005, pp. 1829-1834.

[26] T. Balint and A. D. Lucey, "Instability of a Cantileverd Flexible Plate in Viscous Channel Flow," *Journal of Fluids and Structures*, vol. 20, pp. 893-902, 2005.

[27] L. W. Shayo, "The Stability of Cantilever Panels in Uniform Incompressible Flow," *Journal of Sound and Vibration*, vol. 3, no. 68, pp. 341-350, 1980.

[28] M. J. Lighthill, "Note on Swimming of Slender Fish," *Journal of Fluid Mechanics*, no. 9, pp. 305-317, 1960.

[29] A. D. Lucey and P. W. Carpenter, "The Hydroelastic Stability of Three-Dimensional Disturbance of a Finite Compliant Wall," *Journal of Sound and Vibration*, pp. 527-552, 1993.

[30] C. Eloy, C. Souillez, and L. Schouveiler, "Flutter of a Rectangular Plate," *Journal of Fluids and Structures*, pp. 904-919, 2007.

[31] D. M. Tang, H. Yamamoto, and E. H. Dowell, "Flutter and Limit Cycle Oscillation of Two-Dimensional Panels in Three-Dimensional Axial Flow," *Journal of Fluids and Structures*, vol. 17, pp. 225-242, 2003.

[32] P. J. Attar, E. H. Dowell, and D. M. Tang, "Modelling Aerodynamic Nonlinearity for Two Aeroelastic Configurations: Delta Wing and Flapping Flag," in *44th AIAA/ASME/ASCE/AHS Structures*, Norfolk, VA, 2003, pp. 1-12.

[33] L. Tang and M. P. Païdoussis, "On the Instability and the Post-Critical Behaviour of Two-Dimensional Cantilevered Flexible Plates in Axial Flow," *Journal of Sound and Vibration*, pp. 97-115, 2007.

[34] J. C. Snowdon, *Vibration and Shock in Damped Mechanical Systems*. New York: Wiley, 1968.

[35] E.H. Dowell, *Aeroelasticity of Plates and Shells*. Leyden, Netherlands: Noordhoff International Publishing, 1975.

[36] M.P. Paidoussis, *Fluid-Structure Interactions: Slender Structures and Axial Flow*. London: Academic Press, 1998.

[37] L. Tang and M. P. Païdoussis, "A Numerical Investigation on the Dynamics of Two-Dimensional Cantilevered Flexible Plates in Axial Flow," in *The Sixth FSI, AE & FIV+N Symposium, ASME PVP 2006/ICPVT-11*, Vancouver, 2006.

[38] IEEE Standard on Piezoelectricity, 1987.

[39] A. Erturk and D. J. Inman, "A Distributed Parameter Electromechanical Model for Cantilevered Piezoelectric Energy Harvesters," *Journal of Vibration and Acoustics*, vol. 130, no. 4, pp. 1-15, 2008.

[40] D. J. Inman, *Engineering Vibrations*, #rd ed. New Jersey: Prentice Hall, 2003.

[41] M.P. Païdoussis, *Fluid-Structure Interactions: Slender Structures and*

Axial Flow. London: Academic Press, 1998.

[42] C. Semler, G. X. Li, and M. P. Païdoussis, "The Non-Linear Equations of Motion of Pipes Conveying Fluid," *Journal of Sound and Vibration*, vol. 165, pp. 577-599, 1992.

[43] Sensor Portal. [Online]. http://www.sensorsportal.com

[44] F. M. White, *Fluid Mechanics*, 7th ed. New York, USA: Mc-Graw Hill, 2011.

[45] K. Ogata, *Modern Control Engineering*, 1st ed. Upper Saddle River: Pentice Hall, 1997.